Journal of Power Sources 556 (2023) 232461

Contents lists available at ScienceDirect

Journal of Power Sources

journal homepage: www.elsevier.com/locate/jpowsour

Degradation model of high-nickel positive electrodes: Effects of loss of active material and cyclable lithium on capacity fade

Mingzhao Zhuo *, Gregory Offer, Monica Marinescu

Department of Mechanical Engineering, Imperial College London, London SW7 2AZ, United Kingdom
The Faraday Institution, Didcot OX11 0RA, United Kingdom

HIGHLIGHTS

- Degradation by phase transition of nickel-rich layered NMC oxides to rock-salt phase
- Effects of LAM, LLI, and resistance increase on cyclic capacity and power fade
- High C-rates and degradation inhomogeneity allowed by shrinking-core model within P2D
- Available in open-source package PyBaMM to be coupled with other degradation mechanisms

ARTICLE INFO

Dataset link: https://github.com/mzzhuo/PE_degradation

Keywords:
Battery degradation
Phase transition
Nickel-rich positive electrodes
Degradation mode analysis

ABSTRACT

Nickel-rich layered oxides have been widely used as positive electrode materials for high-energy-density lithium-ion batteries, but the underlying mechanisms of their degradation have not been well understood. Here we present a model at the particle level to describe the structural degradation caused by phase transition in terms of loss of active material (LAM), loss of lithium inventory (LLI), and resistance increase. The particle degradation model is then incorporated into a cell-level P2D model to explore the effects of LAM and LLI on capacity fade in cyclic ageing tests. It is predicted that the loss of cyclable lithium (trapped in the degraded shell) leads to a shift in the stoichiometry range of the negative electrode but does not directly contribute to the capacity loss, and that the loss of positive electrode active materials dominates the fade of usable cell capacity in discharge. The available capacity at a given current rate is further decreased by the additional resistance of the degraded shell layer. The change pattern of the state-of-charge curve provides information of more dimensions than the conventional capacity-fade curve, beneficial to the diagnosis of degradation modes. The model has been implemented into PyBaMM and the source codes are openly available in the GitHub repository https://github.com/mzzhuo/PyBaMM/tree/pe_degradation.

1. Introduction

The pursuit of high energy density has driven the widespread application of layered lithium nickel manganese cobalt (NMC) oxides as positive electrode (PE) materials [1] of lithium ion batteries, especially those with high nickel ratio such as NMC811. However, nickel-rich PEs have been shown to suffer from fast capacity decay and low cycling stability due to a multitude of degradation phenomena, among which a major one is the phase transition from the layered structures to disordered spinel and finally to rock-salt structures at low degrees of lithiation [2]. In this work, we develop a degradation model to account for the PE phase transition and embed it into the Doyle–Fuller–Newman (DFN) model within PyBaMM [3] to quantify the effects of loss of active materials, loss of cyclable lithium, and resistance increase on cell-capacity fade.

Two types of degradation mechanisms have been widely recognized and reported in the literature: structural and chemical decomposition [4]. The first is the structural change through irreversible phase transition of the layered NMC oxides to disordered spinel and rock-salt phases [5,6] that do not have the ability to reversibly intercalate lithium. The phase transition is driven by the fact that the spinel and rock-salt phases are thermodynamically more stable than deintercalated layered oxides [4]. This phase transition is often accompanied with the release of lattice oxygen that eventually leads to formation of oxygen gas (O_2) [7,8]. The subsequent reaction of O_2 with the

* Corresponding author at: Department of Mechanical Engineering, Imperial College London, London SW7 2AZ, United Kingdom.
E-mail addresses: m.zhuo@imperial.ac.uk, mzhuo@connect.ust.hk (M. Zhuo), gregory.offer@imperial.ac.uk (G. Offer), monica.marinescu@imperial.ac.uk (M. Marinescu).

https://doi.org/10.1016/j.jpowsour.2022.232461
Received 16 September 2022; Received in revised form 20 November 2022; Accepted 23 November 2022
Available online 15 December 2022

electrolyte results in other gas byproducts such as CO_2 and CO [7]. The second mechanism of chemical decomposition entails the chemical and electrochemical reactions at the interface between the NMC active material and electrolyte, which is likely to intertwine with the first mechanism of phase transition.

The surface reactions can result in the dissolution of transition metals (TM), such as Ni, Mn, and Co, and the formation of a thin surface layer called pSEI (positive solid electrolyte interphase) [2]. The pSEI layer, consisting of several compounds such as TM fluoride (MF2) and TM carbonates, could impede lithium transport and consume cyclable lithium. The dissolved transition metal ions were found to migrate through the electrolyte and react on the negative electrode (NE) surface, promoting SEI formation at the NE side, thus consuming lithium ions and raising cell impedance [9–11]. Other degradation mechanisms like mechanical fracturing can further impair the performance by exposing newly-formed PE surface to the electrolyte [2] and enabling further structural and chemical degradation.

In spite of the light shed by existing experimental studies, the causes of degradation are still not fully understood [4] due to the complex intertwining of various mechanisms. For example, whether the phase transition or the solid-solution reaction causes the degradation remains an open question [12]. Zhang [8] attributed almost all known problems of NCM811 to the release of lattice oxygen occurring in the irreversible phase transition of layered → spinel → rock-salt structures and suggested to focus on suppression of oxygen evolution in order to mitigate degradation. Ko et al. [1] proposed that the NMC degradation stems from closely-related chemical and structural changes, which cannot be interpreted independently. It becomes apparent that a more thorough understanding of the degradation mechanisms in NMC PEs is urgently needed, including further elucidation from continuing experimental studies.

Meanwhile, modeling studies can help test hypotheses and illuminate the way in which these degradation mechanisms lead to cell capacity fade. Quantitative models can also help in the development of new diagnostic methods, such as those based on degradation mode analysis. Attempts to develop models of PE degradation especially for NMC materials are rare in the literature. Ghosh et al. [13] have recently proposed a shrinking-core model to describe the structural phase transition and oxygen release followed by diffusion through the passivation layer. This model predicts capacity fade during charge by allowing

Acronyms

PE	Positive electrode
OCP	Electrode open circuit potential
LLI_{tot}	Loss of total lithium
LAM_{pe}	Loss of PE active material
DFN	Doyle–Fuller–Newman (or called P2D)
SEI	Solid electrolyte interphase
NE	Negative electrode
LLI	Loss of lithium inventory
LLI_{cyc}	Loss of cyclable lithium
SoC	State of charge
SPM	Single particle model
NMC	Nickel manganese cobalt

Nomenclature

c_p	Variable of lithium concentration in PE active core
c_n	Variable of lithium concentration in NE particle
c_o	Variable of lattice-oxygen concentration in PE shell
s	Variable of core–shell phase boundary location
c_s	Fixed concentration of lithium trapped in PE shell
c_{oc}	Fixed concentration of oxygen stored in PE core
c_e	Lithium-ion concentration in the electrolyte
c_{thrd}	Threshold value of c_p for phase transition
$c_{p,t}$	Top value of c_p corresponding to 0% cell SoC
$c_{p,b}$	Bottom value of c_p corresponding to 100% cell SoC
$c_{p,max}$	Maximum lithium concentration in the PE
$c_{p,surf}$	Surface lithium concentration of PE active core
$c_{n,b}$	Bottom value of c_n corresponding to 0% cell SoC
$c_{n,t}$	Top value of c_n corresponding to 100% cell SoC
$c_{n,max}$	Maximum lithium concentration in the NE
$c_{n,surf}$	Surface lithium concentration of NE particle
D_p	Lithium diffusivity in PE active core
D_o	Lattice-oxygen diffusivity in PE shell
D_n	Lithium diffusivity in NE particles
k_1	Rate constant of forward phase-transition reaction
k_2	Rate constant of backward phase-transition reaction
Q	Nominal cell capacity
I_{app}	Applied current
I	Applied current taken by one PE particle on average
A	Surface area of a single PE particle
$j_{p,ave}$	Averaged interfacial current density in the PE
R	PE particle radius
a	Active particle surface area per unit electrode volume
R_{shell}	Shell-layer resistance
ρ	Shell-layer resistivity
δ	Shell-layer thickness
η_{shell}	Potential drop across the shell layer
$V_{a,p}$	Active material volume in the PE
$V_{a,n}$	Active material volume in the NE
ϵ_s	Volume fraction of active materials
ϵ_e	Volume fraction of electrolyte
$M_{tot,p}$	Total lithium in the PE
$M_{tot,n}$	Total lithium in the NE
M_{tot}	Total lithium in the PE and NE
$M_{tot,0}$	Initial total lithium in the PE and NE
$M_{cyc,p}$	Cyclable lithium in the PE
$M_{cyc,n}$	Cyclable lithium in the NE
M_{cyc}	Cyclable lithium in the PE and NE
$M_{cyc,0}$	Initial cyclable lithium in the PE and NE
j	Interfacial current density
j_0	Exchange current density
k	Rate constant of the charge transfer reaction
ϕ_s	Electric potential of the solid phase
ϕ_e	Electrolyte potential
$\phi'_{e,p}$	Electrolyte potential at PE core–shell boundary
U_{ocp}	Electrode equilibrium potential
σ (σ_{eff})	Bulk (effective) electronic conductivity
D_e ($D_{e,eff}$)	Bulk (effective) diffusivity in the electrolyte
κ (κ_{eff})	Bulk (effective) ionic conductivity
$\kappa_{D,eff}$	Effective diffusional ionic conductivity
f_e	Mean molar activity coefficient
t_e	Transference number
α	Bruggeman exponent
F	Faraday constant
R	Gas constant
T	Absolute temperature

the passivation layer to grow. Lin et al. [14] considered manganese dissolution, electrolyte oxidation, and salt decomposition on the PE and SEI growth and manganese deposition on the NE. Jana et al. [15] considered electrolyte oxidation and chemo-mechanically induced fracture at the PE side.

This paper aims to model the degradation mechanism of phase transition in the PE and its effect on cyclic capacity fade. The irreversible phase transition from the layered to rock-salt structures is universally recognized as an inevitable degradation mechanism [16] especially for nickel-rich layered materials, and it seems to be the most important one because of two observations. Firstly, the electrolyte oxidation and chemical reactions (including pSEI) mainly occur at the beginning of life, much like the SEI formation at the NE side [2], while the phase change and oxygen evolution occur throughout the whole life of the battery [8]. Secondly, the spinel/rock-salt layer has been reported to have thickness of 15–100 nm for a variety of battery chemistries under different usage and storage conditions [17,18], while a surface layer of up to 10 nm [19] was found to build up on the NMC811 PE, which is believed to be the pSEI.

Following the shrinking-core idea to model the phase transition in Ghosh et al. [13], we build a particle degradation model (Section 2) by considering the PE degradation as a progressive growth of rock-salt shell from the particle surface to the center (Fig. 1) in every single PE particle. Compared to Ghosh et al. [13], we present two improvements. Firstly, the particle degradation model is implemented within the DFN model, thus enabling us to account for intermediate/high currents and degradation inhomogeneity across the electrode thickness (Section 4.3). Secondly, we explicitly define the primary degradation modes—loss of active material (LAM), loss of lithium inventory (LLI), and resistance increase—and link them to the phase-transition mechanism. Specifically, the shell layer formed by the phase transition is assumed to constitute the LAM and trap some cyclable lithium that leads to LLI (Section 2.2); it also hinders lithium-ion transport and thus increases the effective cell resistance (Section 2.3) in a similar way to how the SEI layer is often modeled [20]. The primary degradation modes caused by the phase transition are illustrated in Section 4.1 for the purpose of model verification. We then demonstrate the model capability of reproducing experimentally observed phenomena in Section 4.2, focusing on the effects of LAM and LLI on cyclic cell-capacity fade.

2. Degradation model of a single particle

This work models the degradation mechanism of phase transition in the PE at extremely low state of lithiation, equivalent to high cell state of charge (SoC). In this section, we describe a shrinking-core degradation model for a single PE particle; the particle degradation model is then embedded into the DFN model in Section 3 to simulate the cell performance. The spinel/rock-salt phase is assumed to take the form of a shell and expand towards the center of the particle, via a core–shell moving phase boundary. The PE delithiation during cell charge is sketched in Fig. 1 with the phase transition occurring at low stoichiometries, in line with experimental observations [21]. Model *assumptions* are as follows.

- The core denotes the active material remaining the properties at the beginning of life and thus allowing lithium to (de)intercalate within the concentration (stoichiometry) range of $c_{p,b}$ and $c_{p,t}$ in Fig. 1.
- The degraded shell represents the spinel/rock-salt phase, and a fixed amount of lithium (c_s in Fig. 1) gets trapped in the shell; the shell also serves as a lithium-ion conductor with resistance, leading to an overpotential across the shell.
- The (de)intercalation chemical reaction occurs at the core–shell phase boundary with lithium ions supplied through the shell.
- The shell-layer growth rate (inwards moving of the phase boundary) depends on the intercalated lithium concentration and on the lattice-oxygen concentration local to the phase boundary, as shown in Eq. (13).
- The degradation is quantified by LAM, LLI, and increase of the shell-layer resistance.

Based on these assumptions, the governing equations as well as the boundary conditions are outlined in Section 2.1 for a single PE particle; the mass conservation of lithium across the moving phase boundary is used to define the moving-boundary condition. The LAM and LLI induced by the phase transition are defined and calculated in Section 2.2, and the corresponding shell-layer resistance and overpotential are discussed in Section 2.3.

2.1. Governing equations and boundary conditions

In the active core of a PE particle, we consider the diffusion of lithium. As phase transition proceeds at the core–shell phase boundary, lattice oxygen is released and then diffuses out through the shell. The governing equations for lithium diffusion in the core and lattice-oxygen diffusion in the shell are

$$\frac{\partial c_p}{\partial t} + \nabla \cdot \mathbf{h}_p = 0, \tag{1a}$$

$$\frac{\partial c_o}{\partial t} + \nabla \cdot \mathbf{h}_o = 0, \tag{1b}$$

where the mass fluxes of lithium and oxygen are expressed as $\mathbf{h}_p = -D_p \nabla c_p$ and $\mathbf{h}_o = -D_o \nabla c_o$, respectively. At the particle center, the radial symmetry leads to the null-flux boundary condition

$$\mathbf{h}_p|_{r=0} = 0 \tag{2}$$

for the lithium diffusion equation. At the shell outer surface, the oxygen concentration is zero as we assume any oxygen species present there reacts fast:

$$c_o|_{r=R} = 0. \tag{3}$$

The boundary condition for the lithium diffusion equation (1a) at the core–shell phase boundary is derived from lithium conservation across the moving phase boundary as follows. At the core–shell phase boundary, the concentration on the shell side remains constant at c_s as assumed, while the concentration on the core side is the time-dependent variable c_p that is undetermined. Consider Fig. 2a where a thin layer of fresh phase transition is sketched. Recall that the core–shell phase boundary moves towards the particle center with time: at time $t = t_0$, the phase boundary is located at $r = s(t_0)$; later at $t = t_1$, it moves to $r = s(t_1)$. During the small time interval $\Delta t = t_1 - t_0$, a thin layer in the particle, $s(t_1) < r < s(t_0)$, undergoes phase transition from the active core to degraded shell. Meanwhile, the increase of lithium concentration in this layer is $\Delta c(t) = c_s - c_p(t)$, and the total lithium increase is

$$\Delta M = \int_{t_0}^{t_1} 4\pi s^2(t)[-\dot{s}(t)]\Delta c(t)\,\mathrm{d}t, \tag{4}$$

where the time rate of phase-boundary location $\dot{s}(t)$ indicates the speed of the phase transition. Here we introduce the negative sign in front of $\dot{s}(t)$ to ensure a positive volume of the thin layer. According to mass conservation, the increase in total lithium Eq. (4) is equal to the amount of lithium that flows into the layer from both the core and the shell:

$$\Delta M = \int_{t_0}^{t_1} 4\pi s^2(t)\left[\mathbf{h}_p \cdot \mathbf{n}_r + \mathbf{h}_s \cdot (-\mathbf{n}_r)\right]\mathrm{d}t, \tag{5}$$

where $\mathbf{n}_r$ denotes the unit vector along the r direction at the core–shell phase boundary (Fig. 2a). Substituting Eq. (4) into Eq. (5), we have

$$\int_{t_0}^{t_1} 4\pi s^2(t)\left[\dot{s}(t)\Delta c(t) + \mathbf{h}_p \cdot \mathbf{n}_r - \mathbf{h}_s \cdot \mathbf{n}_r\right]\mathrm{d}t = 0. \tag{6}$$

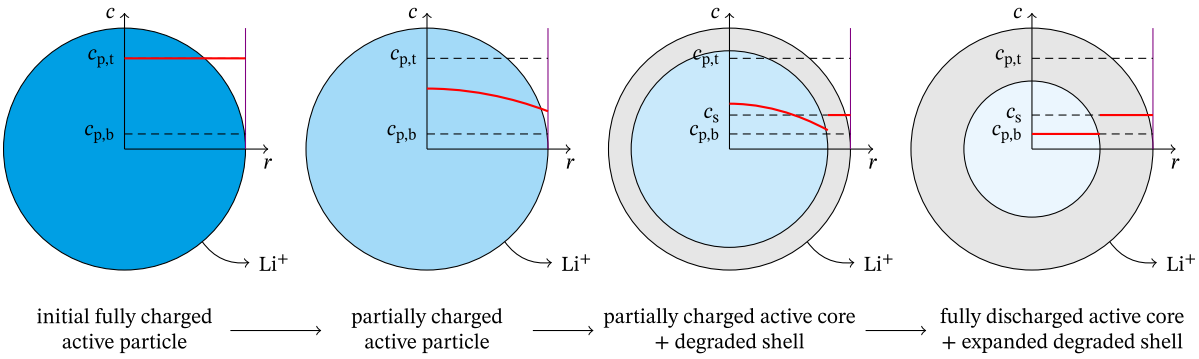

Fig. 1. Schematic showing degradation of a PE particle under delithiation (i.e., cell charge). The degradation advances by the displacement of the phase boundary towards shrinking the core and growing the shell. The active core concentration at 0% cell SoC, the core concentration at 100% cell SoC, and the fixed concentration of lithium trapped in the degraded shell are denoted by $c_{p,t}$, $c_{p,b}$, and c_s. This schematic is inspired by Ref. [22] in terms of demonstration of the delithiation process.

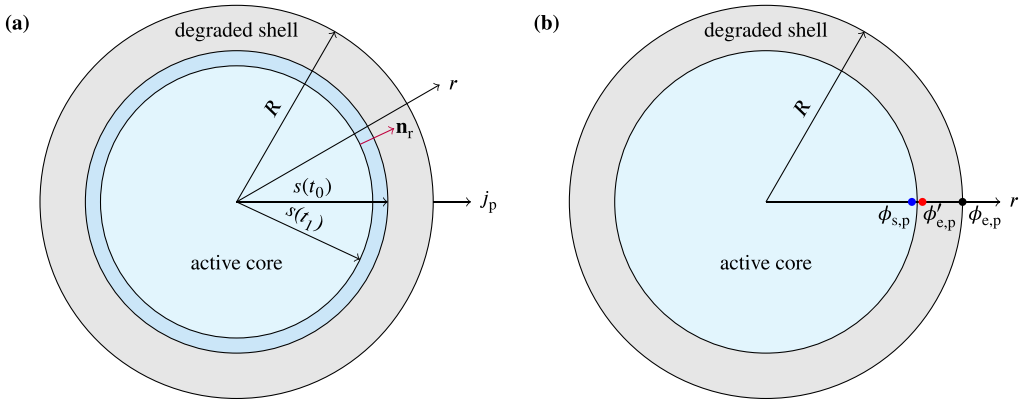

Fig. 2. Schematic of the shrinking-core degradation model for a PE particle. The core represents the active material while the shell denotes the degraded surface layer due to phase transition. (a) The displacement of the core–shell phase boundary within a small time interval $\Delta t = t_1 - t_0$ from $r = s(t_0)$ to $r = s(t_1)$, associated with a thin layer of active materials transformed into rock-salt shell. Symbol $\mathbf{n}_r$ denotes the unit vector along the r direction, and j_p represents the interfacial current density leaving the particle. (b) Illustration of the shell-layer overpotential and the potentials used in Butler–Volmer equation: $\phi_{s,p}$ (blue point) is the electric potential of the electronically conductive solid phase, $\phi'_{e,p}$ (red point) is the electrolyte potential at the core–shell phase boundary, and $\phi_{e,p}$ (black point) is the electrolyte potential at the shell outer surface.

Because the above equation holds for all intervals of integration $[t_0, t_1]$, it follows that the integrand must vanish identically:

$$\dot{s}(c_s - c_p) + \mathbf{h}_p \cdot \mathbf{n}_r - \mathbf{h}_s \cdot \mathbf{n}_r = 0. \tag{7}$$

In Eq. (7), the flux term from the core side can be expressed as

$$\mathbf{h}_p \cdot \mathbf{n}_r = -D_p \frac{\partial c_p}{\partial r} \mathbf{n}_r \cdot \mathbf{n}_r = -D_p \frac{\partial c_p}{\partial r}, \tag{8}$$

and the flux term associated with the shell phase is related to the interfacial current density according to mass conservation in the shell:

$$\mathbf{h}_s \cdot \mathbf{n}_r = (R/s)^2 \frac{j_p}{F}, \tag{9}$$

where the interfacial current density j_p is positive when lithium leaves the PE particle and F is Faraday constant. Inserting Eqs. (8) and (9) into Eq. (7), we arrive at

$$\dot{s}(c_s - c_p) - D_p \frac{\partial c_p}{\partial r} - (R/s)^2 \frac{j_p}{F} = 0. \tag{10}$$

Following the same procedures, we can obtain the boundary condition for Eq. (1b) at the core–shell phase boundary via lattice-oxygen conservation across the moving phase boundary. Analogous to Eq. (7), for oxygen conservation we have

$$\dot{s}(c_o - c_{oc}) - \mathbf{h}_o \cdot \mathbf{n}_r = 0, \tag{11}$$

where c_{oc} is the fixed concentration of oxygen in the core stored in the form of oxide compounds, and c_o is the time-dependent variable at the phase boundary on the shell side. This relation suggests that the phase transition and chemical reactions release the stored oxygen in the core into lattice oxygen that will diffuse out through the shell. Applying the same operation as in Eq. (8), we can reformulate $\mathbf{h}_o \cdot \mathbf{n}_r$ and rewrite Eq. (11) as

$$\dot{s}(c_o - c_{oc}) + D_o \frac{\partial c_o}{\partial r} = 0. \tag{12}$$

We remark that the time-dependent variables c_p and c_o are unknowns at $r = s(t)$, and thus the two boundary conditions (10) and (12) are of Robin type, expressing mass conservation of lithium and oxygen across the moving core–shell phase boundary.

To complete Eqs. (10) and (12), the speed of phase transition $\dot{s}$ needs to be specified. The inwards moving of the phase boundary intrinsically depends on the lithium and oxygen concentrations at the boundary, as well as on the temperature. The ambient temperature has been observed to accelerate degradation [23]. Due to a distinct lack of experimental data for any validation, we ignore the temperature effect and model the degradation progress at an accelerated rate. In particular, the speed of phase transition is taken from Ghosh et al. [13]:

$$\dot{s} = \begin{cases} -(k_1 - k_2 c_o), & \text{if } c_p < c_{thrd}; \\ 0, & \text{otherwise}, \end{cases} \tag{13}$$

where c_p and c_o take values at $r = s(t)$, k_1 and k_2 are the rate constants of the forward and backward reactions, and c_{thrd} is the threshold value below which phase transition occurs.

2.2. LAM and LLI

The degradation mechanism of phase transition in a high-nickel PE leads to loss of PE active material (LAM_{pe}) and loss of lithium inventory

(LLI). In the current work, we assume the shell phase has no ability to store lithium and thus provides no capacity; instead, it remains as a lithium-ion conductor only. The $\mathrm{LAM_{pe}}$ is thus defined as the volume fraction of the shell phase over the whole particle:

$$\mathrm{LAM_{pe}} = 1 - \frac{V_{\mathrm{core}}}{V_{\mathrm{particle}}} = 1 - \left(\frac{s}{R}\right)^3, \tag{14}$$

where $V_{\mathrm{core}} = 4\pi s^3/3$ is the volume of the active core and $V_{\mathrm{particle}} = 4\pi R^3/3$ denotes the particle volume.

The LLI is defined through the difference between the current lithium content and the initial content in both PE and NE. By convention, the lithium content refers to the total lithium $M_{\mathrm{tot}} = M_{\mathrm{tot,p}} + M_{\mathrm{tot,n}}$ in the electrodes and is calculated as follows:

$$M_{\mathrm{tot,p}} = c_{\mathrm{p}} \times (1 - \mathrm{LAM_{pe}}) \times V_{\mathrm{a,p}}, \tag{15a}$$

$$M_{\mathrm{tot,n}} = c_{\mathrm{n}} \times V_{\mathrm{a,n}}, \tag{15b}$$

where c_{p} and c_{n} represent lithium concentrations in the positive core and the negative particle, respectively, and V_{a} is the active material volume in the PE ("p") and NE ("n"). The LLI in terms of total lithium is then defined as

$$\mathrm{LLI_{tot}} = 1 - \frac{M_{\mathrm{tot}}}{M_{\mathrm{tot,0}}} = 1 - \frac{M_{\mathrm{tot,p}} + M_{\mathrm{tot,n}}}{M_{\mathrm{tot,p,0}} + M_{\mathrm{tot,n,0}}}, \tag{16}$$

where the subscript "0" indicates the initial state. As the phase transition proceeds, the degraded shell layer grows and traps more lithium that cannot be used in cycling. Therefore, the total lithium decreases with the phase transition, and thus $\mathrm{LLI_{tot}}$ is always nonzero if the phase transition occurs.

Note that not all the lithium stored in the active materials shuttle between the PE and NE. As shown in Fig. 3, the experimental operating protocol determines the 0% and 100% cell SoCs, and the difference between them represents the cyclable lithium. At the beginning of life, the top value $c_{\mathrm{p,t}}$ of lithium concentration in the PE paired with the bottom value $c_{\mathrm{n,b}}$ of concentration in the NE (shaded in light blue) yields the condition for 0% SoC, while the bottom value $c_{\mathrm{p,b}}$ in the PE paired with the top value $c_{\mathrm{n,t}}$ in the NE (light pink) yields the condition for 100% SoC. The amount of lithium below $c_{\mathrm{p,b}}$ (also $c_{\mathrm{n,b}}$) is not cycled between the PE and NE due to the experimental protocol. Thus, the loss of this non-cyclable lithium into dead lithium upon shell formation has no impact on the cell performance. Only the loss of cyclable lithium translates into reduced capacity of the cell. We further define the total cyclable lithium, based on the 0% and 100% SoCs, as

$$M_{\mathrm{cyc,p}} = (c_{\mathrm{p}} - c_{\mathrm{p,b}}) \times (1 - \mathrm{LAM_{pe}}) \times V_{\mathrm{a,p}}, \tag{17a}$$

$$M_{\mathrm{cyc,n}} = (c_{\mathrm{n}} - c_{\mathrm{n,b}}) \times V_{\mathrm{a,n}}, \tag{17b}$$

where the bottom limit value $c_{\mathrm{p,b}}$ ($c_{\mathrm{n,b}}$) is deducted from the real-time concentration c_{p} (c_{n}), as this amount of lithium is not cycled. The corresponding LLI in terms of total cyclable lithium is

$$\mathrm{LLI_{cyc}} = 1 - \frac{M_{\mathrm{cyc}}}{M_{\mathrm{cyc,0}}} = 1 - \frac{M_{\mathrm{cyc,p}} + M_{\mathrm{cyc,n}}}{M_{\mathrm{cyc,p,0}} + M_{\mathrm{cyc,n,0}}}. \tag{18}$$

Note that the top and bottom values are different from the maximum and minimum concentrations that are determined by the active material itself rather than experimental protocols.

The transition to spinel/rock-salt phase has been observed to occur predominantly when the lithium concentration in the PE is low (see Eq. (13)). Therefore, the amount of lithium trapped in the shell, denoted as c_{s}, is also expected to be low. If c_{s} equals $c_{\mathrm{p,b}}$, we infer that the $\mathrm{LLI_{cyc}}$ in Eq. (18) will be zero, although $\mathrm{LLI_{tot}}$ in Eq. (16) is positive. Because of no loss of cyclable lithium, the cell performance is not affected. If c_{s} is not equal to $c_{\mathrm{p,b}}$, the cyclable lithium may increase or decrease, resulting in negative or positive $\mathrm{LLI_{cyc}}$, respectively.

2.3. Shell resistance and overpotential

As the shell is assumed not to store lithium, the intercalation reaction occurs at the core–shell phase boundary. Meanwhile, the shell layer is assumed to be ion-conductive so that lithium ions can be transferred to the core surface. This transfer process results in a potential drop across the shell layer, which affects the calculation of overpotential for interfacial current density. The approach to modeling the shell-layer effects is similar to the conventional treatment of the SEI layer at the NE side [20].

We assume that the resistivity of the shell layer, denoted as ρ, is constant and uniform. Since the shell is generally thin for a working cell, we approximate it as a flat shell with thickness $\delta = R - s$ and surface area $A = 4\pi R^2$. The shell-layer resistance is formulated as

$$R_{\mathrm{shell}} = \frac{\rho\delta}{A}, \tag{19}$$

and the potential drop across the shell is

$$\eta_{\mathrm{shell}} = I R_{\mathrm{shell}} = \rho\delta j_{\mathrm{p,ave}}, \tag{20}$$

where I denotes the averaged current flowing into the electrolyte from a single PE particle and $j_{\mathrm{p,ave}} = I/A$ is the averaged interfacial current density.

By convention, we use the Butler–Volmer equation to describe the intercalation reaction at the PE active core surface, and the interfacial current density j_{p} is expressed as

$$j_{\mathrm{p}} = j_{0,\mathrm{p}}\left[\exp\left(\frac{0.5F}{RT}\eta_{\mathrm{p}}\right) - \exp\left(-\frac{0.5F}{RT}\eta_{\mathrm{p}}\right)\right], \tag{21}$$

where $j_{0,\mathrm{p}}$ is the exchange current density and η_{p} is the reaction overpotential. The current density j_{p} is defined with a positive value when lithium leaves the PE active material particles. The exchange current density j_0 is given by

$$j_{0,\mathrm{p}} = kF c_{\mathrm{p,surf}}^{0.5}\left(c_{\mathrm{p,max}} - c_{\mathrm{p,surf}}\right)^{0.5} c_{\mathrm{e}}^{0.5}, \tag{22}$$

where k $\left(\mathrm{m^{2.5}\ mol^{-0.5}\ s^{-1}}\right)$ is the rate constant of the charge transfer reaction, $c_{\mathrm{p,max}}$ is the maximum saturation concentration of intercalated lithium, $c_{\mathrm{p,surf}}$ is the surface lithium concentration of the active core, and c_{e} is the lithium ion concentration in the electrolyte.

Referring to Fig. 2b, the reaction overpotential η_{p} at the PE in Eq. (21) is expressed, by definition, as

$$\eta_{\mathrm{p}} = \phi_{\mathrm{s,p}} - \phi'_{\mathrm{e,p}} - U_{\mathrm{ocp,p}},$$

where the PE equilibrium potential $U_{\mathrm{ocp,p}}$ is a function of the surface concentration $c_{\mathrm{p,surf}}$ of the active core, and $\phi_{\mathrm{s,p}}$ is the electric potential of the solid phase in the PE. Following the approach of Safari et al. [20] when addressing the SEI layer overpotential, we relate the electrolyte potential ϕ'_{e} at the core–shell phase boundary to the electrolyte potential ϕ_{e} at the shell outer surface via

$$\phi'_{\mathrm{e,p}} = \phi_{\mathrm{e,p}} + \eta_{\mathrm{shell}}. \tag{23}$$

Thus, the PE reaction overpotential η_{p} in Eq. (21) can now be expressed as

$$\eta_{\mathrm{p}} = \phi_{\mathrm{s,p}} - \phi_{\mathrm{e,p}} - \eta_{\mathrm{shell}} - U_{\mathrm{ocp,p}}. \tag{24}$$

3. Full-cell model

The particle degradation model developed in Section 2 describes a single particle in the PE. In order to estimate the cell degradation, this model is then embedded into a cell-level model such as the DFN model. The remaining equations of the DFN model are outlined in the following (Sections 3.1 and 3.2) for completeness. For more details of the DFN model, readers are referred to the literature [24,25].

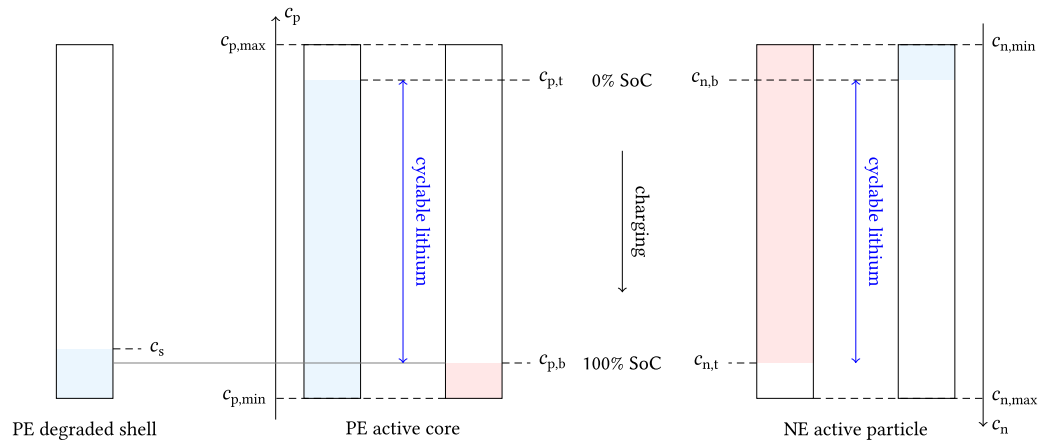

Fig. 3. Illustration for the cyclable lithium shutting between the PE and NE. With the cell SoC varying between 0 and 100%, the lithium concentration c_p in the PE particle varies between two limit values $[c_{p,b}, c_{p,t}]$, and the concentration c_n in the NE particle varies within $[c_{n,b}, c_{n,t}]$. The 0% cell SoC is defined by $c_{p,t}$ in the PE together with $c_{n,b}$ in the NE, while the 100% cell SoC is defined by $c_{p,b}$ in the PE with $c_{n,t}$ in the NE. The concentration of trapped lithium in the degraded shell layer is constant at c_s, which is comparable to $c_{p,b}$.

3.1. Lithium diffusion in negative particles

We consider no degradation in the NE, and thus fickian diffusion is modeled for each NE particle. The governing equation reads

$$\frac{\partial c_n}{\partial t} + \nabla \cdot \left(-D_n \nabla c_n\right) = 0, \tag{25}$$

where D_n is the diffusivity of intercalated lithium in negative particles.

Radial symmetry dictates that the same Neumann boundary condition as in Eq. (2) applies to Eq. (25). At the particle surface, the following Neumann boundary condition is applied

$$-D_n \frac{\partial c_n}{\partial r} = j_n / F, \tag{26}$$

where the interfacial current density is also obtained through Butler–Volmer equation and its expression is readily available in the literature [24,25].

3.2. Conservation equations at cell level

A cell consists of the NE, separator, and the PE. At the cell level, both the NE and PE consist of a solid phase with electronic conduction (ϕ_s) and an electrolyte phase with ionic conduction (ϕ_e) and lithium-ion transport (c_e). For the separator we only need to model the electrolyte phase in a porous medium. The conservation of electric charge in the solid phase of the two electrodes results in the relation

$$\nabla \cdot \left(-\sigma_{eff} \nabla \phi_s\right) = -aj, \tag{27}$$

where σ_{eff} and ϕ_s denote the effective electronic conductivity and electric potential inside the electrode phase, respectively. Quantity j is the interfacial current density from the active particle to the electrolyte (charge sink), and a denotes the active particle surface area per unit electrode volume:

$$a = \frac{4\pi R^2}{4\pi R^3/3}\epsilon_s = \frac{3\epsilon_s}{R}, \tag{28}$$

where ϵ_s denotes the active material volume fraction and R the active particle radius. The conservation of lithium ions in the electrolyte phase of the whole cell (two electrodes and separator) can be expressed as

$$\epsilon_e \frac{\partial c_e}{\partial t} + \nabla \cdot \left(-D_{e,eff}\right) \nabla c_e = \left(1 - t_e\right) a \frac{j}{F}, \tag{29}$$

where c_e denotes the lithium-ion concentration, ϵ_e is the volume fraction of electrolyte phase, $D_{e,eff}$ is the effective diffusivity in the electrolyte, and t_e is the lithium-ion transference number. The conservation of electric charge in the electrolyte phase of the whole cell is written as

$$\nabla \cdot \left(-\kappa_{eff} \nabla \phi_e + \kappa_{D,eff} \nabla \ln c_e\right) = aj, \tag{30}$$

where κ_{eff} is the effective ionic conductivity, ϕ_e is the electric potential in the electrolyte, and $\kappa_{D,eff}$ is the effective diffusional conductivity expressed as

$$\kappa_{D,eff} = \frac{2RT\kappa_{eff}}{F}\left(1 + \frac{\partial \ln f_e}{\partial \ln c_e}\right)\left(1 - t_e\right), \tag{31}$$

where T is the temperature and f_e is the mean activity coefficient. The effective electronic conductivity σ_{eff}, effective electrolyte diffusivity $D_{e,eff}$, and ionic conductivity κ_{eff} are related to corresponding bulk properties through the Bruggeman correlation [26]:

$$\sigma_{eff} = \sigma\epsilon_s^{\alpha}, \quad D_{e,eff} = D_e\epsilon_e^{\alpha}, \quad \kappa_{eff} = \kappa\epsilon_e^{\alpha},$$

where α is the Bruggeman exponent, and σ, D_e, and κ are bulk material properties that can be concentration dependent.

3.3. Cell voltage

The DFN model resolves the variation of field variables in the through-cell direction and thus is especially needed for (dis)charges at a high-current rate where the lithium-ion concentration gradient in the electrolyte cannot be ignored. However, for the cases where averaged quantities over the electrode thickness are sufficient to describe the cell performance, a suitable choice is the SPM. The same PE phase-transition model as described in the previous section can be embedded into any given SPM, should the latter be preferred. The fickian diffusion model for the PE particle in the SPM would be replaced by the developed particle degradation model. The simplification from the DFN model to SPM can be found for example in Marquis et al. [25], and here we just detail the cell terminal voltage calculation in the SPM for better interpretation of the following simulation results.

Similar to the PE reaction overpotential in Eq. (24), the NE reaction overpotential is expressed as

$$\eta_n = \phi_{s,n} - \phi_{e,n} - U_{ocp,n}, \tag{32}$$

except for the shell overpotential term η_{shell}. The difference between the solid-phase potential of the PE and that of the NE is defined as the cell terminal voltage and can be obtained by subtracting the two Eqs. (24) and (32):

$$V_t = \phi_{s,p} - \phi_{s,n} = U_{ocp,p}\left(c_{p,surf}\right) - U_{ocp,n}\left(c_{n,surf}\right) + \eta_p - \eta_n + \eta_{shell}. \tag{33}$$

Note that in the SPM, we ignore the electrolyte effect and consider equal electrolyte potentials $\phi_{e,p} = \phi_{e,n}$ in the PE and NE.

Table 1
Parameter values for simulation of a commercial lithium-ion cell with NMC811 positive electrode (PE) and SiC negative electrode (NE).

Parameter	Symbol	Unit	Value		Note/Ref.
			PE (i = p)	NE (i = n)	
Particle radius	R_i	μm	3.8	6.1	[27]
Active material volume fraction	ϵ_s	–	0.745	0.694	[27]
Electrolyte volume fraction (porosity)	ϵ_e	–	0.171	0.216	[27]
Maximum lithium concentration	$c_{i,\max}$	mol/m^3	49 340	34 257	[13]
Stoichiometry at 0% SoC[a]	$c_i/c_{i,\max}$	–	0.942	0.002	[13]
Stoichiometry at 100% SoC[a]	$c_i/c_{i,\max}$	–	0.222	0.852	[13]
Diffusivity	D_i	m^2/s	1.0×10^{-14}	1.0×10^{-14}	[13]
Charge-transfer reaction rate	k	m$^{2.5}$ mol$^{-0.5}$ s^{-1}	3.2×10^{-11}	1.0×10^{-11}	[13]
Electronic conductivity	σ	m^2/s	0.17	100	[27]
Electrode thickness	L_{ed}	μm	86.7	66.2	[27]
Open circuit potential	U_{ocp}	V	data[b]	data[b]	[27]
Initial concentration	$c_{i,0}$	mol/m^3	46 478.28	68.514	0% SoC
Initial oxygen concentration in PE shell	$c_{o,0}$	mol/m^3	0		
Initial phase boundary location	s_0	μm	3.75		
Threshold value for phase transition	c_{thrd}	mol/m^3	14 802		0.3 $c_{p,\max}$
Fixed oxygen concentration in the core	c_{oc}	mol/m^3	152 193.21		[13]
Oxygen diffusivity in the shell	D_o	m^2/s	1×10^{-17}		[13]
Forward reaction rate constant	k_1	m/s	0.8544×10^{-11}		[13]
Reverse reaction rate constant	k_2	m^4/mol/s	1.732×10^{-16}		[13]
PE shell resistivity	ρ	Ω m	1×10^6		[20][c]
Nominal cell capacity	Q	A h	3.35		[13,27]
Lower cut-off voltage	V_{lower}	V	2.8		
Upper cut-off voltage	V_{upper}	V	4.2		
Current collector/electrode interface area	A_{cc}	m^2	7.134×10^{-2}		[13]
Lithium-ion concentration in electrolyte	c_e	mol/m^3	1000		PyBaMM[d]
Electrolyte diffusivity	D_e	m^2/s	$5.34\times10^{-10}\,e^{-0.65c_e}$		[28]
Ionic conductivity	κ	S/m	$0.0911+1.9101c_e-1.052c_e^2+0.1554c_e^3$		[28]
Transference number	t_e	–	0.4		PyBaMM[d]
Thermodynamic factor	$1+\partial\ln f_e/\partial\ln c_e$	–	1		PyBaMM[d]
Separator porosity	ϵ_e	–	0.45		PyBaMM[d]
Separator thickness	L_{sep}	μm	12		[27]
Faraday constant	F	C/mol	96 485		
Gas constant	R	J/(K mol)	8.31		
Absolute temperature	T	K	298.15		
Bruggeman exponent	α	–	1.5		[27]

[a]See Fig. 3.
[b]Refer to Fig. 2a and b in Sturm et al. [27] for electrode OCP curves and the link therein to download the data.
[c]Estimated based on a SEI layer resistivity.
[d]Open-source repository: https://github.com/pybamm-team/PyBaMM.

4. Results and discussion

This section demonstrates the capability of the proposed model to describe the LAM_{pe}, LLI_{cyc}, and shell-layer resistance R_{shell}, as well as their contribution to the cell capacity fade. We first demonstrate in Section 4.1 that the model performs as expected in the case of calendar ageing. Then, we run cyclic ageing tests to demonstrate effects of the LAM_{pe}, LLI_{cyc}, and R_{shell} on the capacity fade in Section 4.2. In the first two sections, we choose the Single Particle Model (SPM in PyBaMM) to accommodate the particle degradation model because the focus is to analyze the overall response of the electrode at low current rates. We then plug the particle degradation model into the DFN model (DFN in PyBaMM) to demonstrate degradation inhomogeneity in the electrode thickness direction at medium and high current rates (Section 4.3).

The parameter values for the numerical simulation are taken from Sturm et al. [27] and Ghosh et al. [13] for a commercial lithium-ion cell (INR18650-MJ1, LG Chem) with NMC811 cathode and SiC anode. Note that the parameters associated with the phase transition are exaggerated to accelerate the degradation in the tests of calendar and cyclic ageing for the sake of computational cost reduction. These parameter values are listed in Table 1.

4.1. LAM and LLI in calendar ageing

In this section, we quantify three degradation modes—the LAM_{pe}, LLI_{cyc}, and shell resistance—in the scenario of calendar ageing at a high cell voltage (low level of PE lithiation). The LAM_{pe} and shell resistance are directly calculated from Eqs. (14) and (19), respectively, depending on the shell-layer thickness. However, the LLI_{cyc} defined in Eq. (18) does not show a straightforward dependence on the extent of degradation and thus needs further numerical studies. We assumed that the lithium present in the degraded shell is fixed at a constant concentration level c_s and is indefinitely trapped such that it no longer contributes to the cell capacity. The parameter c_s is a key factor impacting the calculation of LLI_{cyc} via the mass conservation across the core–shell phase boundary as expressed in Eq. (10). To understand how cyclable lithium is lost, we investigate the effect of the parameter c_s.

The model is run for the following scenario: from fully discharged, the cell is charged at a low constant-current rate (0.5 C) until the upper cut-off voltage of 4.2 V; the cell is then stored for 6 h, enabling degradation to occur. Three cases regarding the value of c_s are considered: (I) $c_s = 0.182\,c_{p,\max} < c_{p,b}$, (II) $c_s = 0.222\,c_{p,\max} = c_{p,b}$, and (III) $c_s = 0.324\,c_{p,\max} > c_{p,b}$.

As shown in Fig. 4, the storage starts at $t = 2.34$ h and ends at $t = 8.34$ h. The degradation is triggered at the end of the charge ($t = 1.62$ h) when the lithium concentration drops below the threshold value according to Eq. (13). Fig. 4a shows the current profile, confirming the protocol specified above. Since the parameter c_s does not affect the progress of phase transition, the core–shell phase boundary s/R and the LAM_{pe} evolve in identical ways for all three cases, as shown in Fig. 4b–c: they remain at the values of the initial conditions until the PE degradation starts at $t = 1.62$ h, after which s/R decreases as the shell thickens and the LAM_{pe} increases accordingly.

The LLI including LLI_{tot} and LLI_{cyc} are shown in Fig. 4e–g for all three cases. Since the lithium trapped in the shell is considered as a pure

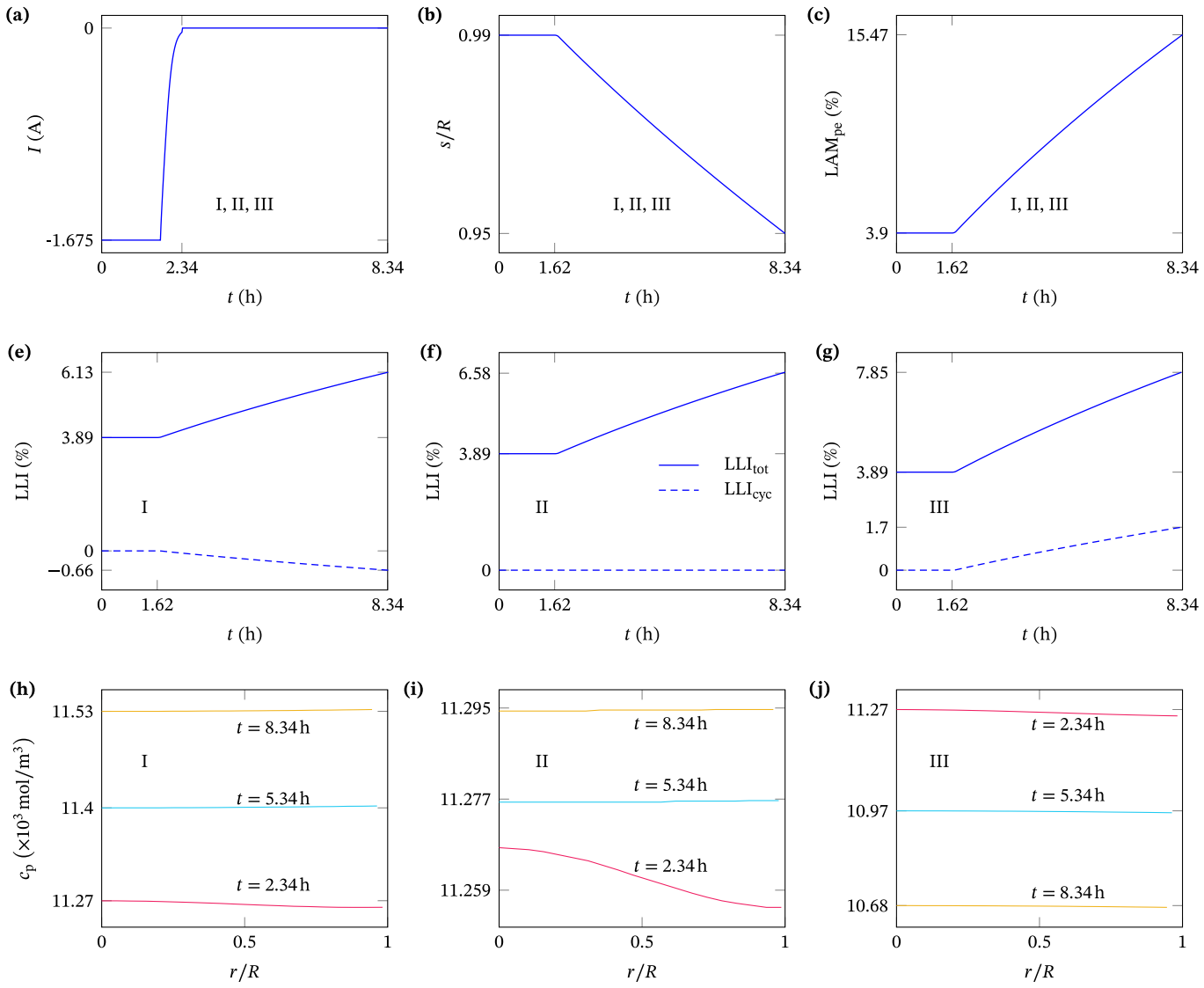

Fig. 4. Effects of the trapped lithium content c_s on the loss of total lithium $\mathrm{LLI_{tot}}$ and loss of total cyclable lithium $\mathrm{LLI_{cyc}}$. Three cases are considered: (I) $c_s = 0.182\, c_{p,max} < c_{p,b}$, (II) $c_s = 0.222\, c_{p,max} = c_{p,b}$, and (III) $c_s = 0.324\, c_{p,max} > c_{p,b}$. The experimental protocol is the same for all three cases, and so is the applied current I (a). The phase boundary location s (b) and $\mathrm{LAM_{pe}}$ (c) are the same for all three cases, as they do not depend on c_s. The LLI evolution and lithium concentration c_p at three time instants during the 6-hour rest are plotted for case (I) in subplots (e) and (h), for case (II) in subplots (f) and (i), and for case (III) in subplots (g) and (j).

loss, it is excluded in the total lithium calculation in Eq. (15a) via the deduction of $\mathrm{LAM_{pe}}$. Hence, the $\mathrm{LLI_{tot}}$ is always positive and increases with degradation. From case (I) to (III), we can see that the higher the c_s value, the greater the $\mathrm{LLI_{tot}}$, in spite of the same degradation and shell volume growth for all three cases. Note that the initial value is the same at 3.89% because the same amount of lithium loss is considered for the initial shell of nonzero thickness.

In contrast, the $\mathrm{LLI_{cyc}}$ varies depending on the value of c_s relative to that of $c_{p,b}$: it decreases with progressive phase transition when $c_s < c_{p,b}$ (case I), suggesting that extra cyclable lithium is harvested due to the phase transition; when $c_s > c_{p,b}$ (case III), the $\mathrm{LLI_{cyc}}$ is positive and increases with the degradation; if $c_s = c_{p,b}$ (case II), the $\mathrm{LLI_{cyc}}$ remains null, regardless of the phase transition occurring. The explanation is as follows. In the core, the lithium below the level $c_{p,b}$ (corresponding to 100% SOC in Fig. 3) is not cycled and temporarily gets "trapped" in the core; only the rest lithium above the concentration $c_{p,b}$ is taken into account in the calculation of total cyclable lithium (Eq. (17a)). Consider the transition of a thin layer of active core to the shell phase (see Fig. 2a). When $c_s = c_{p,b}$, the "trapped" lithium (up to $c_{p,b}$) in the thin layer of active core just continues to be trapped in the shell after the transition, while all the remaining cyclable lithium is pushed to the untransformed active core due to the mass conservation across the phase boundary. In this process, there is no loss and gain of cyclable lithium. If $c_s > c_{p,b}$, some cyclable lithium from the active core, including the thin layer, will be consumed to fill the gap between c_s and $c_{p,b}$, leading to positive $\mathrm{LLI_{cyc}}$. If $c_s < c_{p,b}$, some part of the "trapped" lithium in the thin layer of active core, together with the rest cyclable lithium, is transferred to the remaining active core and thus remains cyclable. We remark that the harvest of cyclable lithium in case I seems counter-intuitive but does not violate physics.

The variation of lithium concentration c_p in PE active core is shown in Fig. 4h–j as the phase transition proceeds. After the voltage control ($t = 2.34$ h), the concentration c_p in the active core is approximately equal to $11.27\,\mathrm{kmol/m^3}$, which is higher than $c_{p,b} = 10.95\,\mathrm{kmol/m^3}$ that corresponds to the 100% cell SoC. In cases I and II, the values of c_s are $9\,\mathrm{kmol/m^3}$ and $10.95\,\mathrm{kmol/m^3}$, respectively, both lower than $c_p = 11.27\,\mathrm{kmol/m^3}$ in the core. As the phase transition occurs, the difference between c_p and c_s is transferred to the untransformed core due to the mass conservation law. As a result, the lithium concentration c_p in the untransformed core increases slightly during the phase transition—see

the concentration profiles at three time instants in Fig. 4h and i. However, in case (III), $c_s = 16\,\mathrm{kmol/m^3}$ is higher than $c_p = 11.27\,\mathrm{kmol/m^3}$ in the core. The lithium is thus transferred from the untransformed core to the newly-formed shell to fill the concentration gap, and the lithium concentration c_p in the untransformed core decreases accordingly with time as shown in Fig. 4j. In conclusion, the lithium concentration in the active core evolves depending on its value relative to the value of c_s, unlike the $\mathrm{LLI_{cyc}}$.

4.2. Capacity fade in cyclic ageing

In the previous section, we demonstrated that the phase transition causes the $\mathrm{LAM_{pe}}$, $\mathrm{LLI_{cyc}}$, and shell resistance, and in this section we run cyclic tests to explore their effects on cell capacity fade. The cyclic ageing tests in our simulations are defined to closely resemble experimental ones, and a typical cycle is specified as

Charge at 0.5 C until 4.2 V,
Hold at 4.2 V until C/50,
Rest for 60 min,
Discharge at 0.5 C until 2.8 V,
Hold at 2.8 V until C/50,
Rest for 60 min.

According to Eq. (13), the degradation mainly occurs at low lithiation levels in the PE. The voltage control and rest are thus added after the constant-current charge to allocate more time for degradation. Also, an accelerated degradation rate, rather than a real-world one, is used to reduce the simulation cost. A total of 20 consecutive cycles are repeated for three simulated scenarios: (I) only $\mathrm{LAM_{pe}}$, (II) $\mathrm{LAM_{pe}}$ and $\mathrm{LLI_{cyc}}$, and (III) $\mathrm{LAM_{pe}}$, $\mathrm{LLI_{cyc}}$, and shell resistance.

The results of scenario I are shown in Fig. 5 to explore the effects of $\mathrm{LAM_{pe}}$ exclusively. In this case, we set the parameter $c_s = c_{p,b}$ so that there is no loss of cyclable lithium and set $\rho = 0$ to remove the shell resistance and overpotential across the shell layer. The calculated $\mathrm{LLI_{cyc}}$ is zero, as can be directly seen in Fig. 5c or be cross-checked by the constant total cyclable lithium $M_{cyc} = M_{cyc,p} + M_{cyc,n}$ in both the PE and NE as shown in Fig. 5e.

In Fig. 5a, the normalized phase boundary location s/R decreases with time, indicating the phase transition occurs towards the particle center as designed. However, it does not decreases at all times, and this is because of the condition specified in Eq. (13) that the phase transition only occurs when the core surface concentration is lower than the threshold value. Hence, the phase transition occurs and the phase boundary location decreases mainly at the end of cell charge and in the following voltage hold and rest. Correspondingly, the $\mathrm{LAM_{pe}}$ increases with time (Fig. 5b) in a similar fashion to the phase boundary location, as governed by Eq. (14). Note that we specify a nonzero initial shell thickness to avoid numerical issues arising in the transformation of computational domains, e.g., a zero denominator in Eq. (A.1).

Fig. 5d shows the evolution of the cell SoC, which is calculated through Coulomb counting:

$$\mathrm{SoC} = -\frac{1}{Q}\int_0^t I_{app}(t)\,\mathrm{d}t\,, \tag{34}$$

where Q is the nominal capacity and I_{app} is the applied current with positive sign on discharge. As a cycle begins, the SoC first increases during the charge and the following voltage control, and then it stays constant in the rest; in the latter half of a cycle, the SoC decreases during the discharge and voltage control and then stays unchanged during the rest. This variation pattern is repeated from cycle to cycle. However, the SoC upper limit stays unchanged, while the lower limit increases with the cycle number. The SoC range is thus shrinking, leading to cell capacity fade.

The shrinkage of the SoC range is due to the phase-transition-induced degradation, and the specific change pattern is caused by the increasing $\mathrm{LAM_{pe}}$ and zero $\mathrm{LLI_{cyc}}$, as explained below. At the end of charge, all the cyclable lithium is supposed to shuttle into the NE. In our model, the NE does not degrade and thus can accommodate all the cyclable lithium, regardless of the cycle number. In this scenario, there is no loss of cyclable lithium; therefore, the SoC upper limit at the end of charge does not vary with cycle number. This is also confirmed by the unvarying upper limit of cyclable lithium $M_{cyc,n}$ in the NE in Fig. 5e that equals the total cyclable lithium M_{cyc}. Now consider the other side. As a discharge starts, the cyclable lithium is transferred back to the PE. However, due to the $\mathrm{LAM_{pe}}$, the PE is not able to accommodate all the cyclable lithium. The more severe degradation, the greater $\mathrm{LAM_{pe}}$, the less lithium the PE can accommodate, and the more lithium left in the NE at the end of discharge. This is verified by the observation in Fig. 5e that the upper limit of cyclable lithium $M_{cyc,p}$ in the PE decreases, while the lower limit of cyclable lithium $M_{cyc,n}$ in the NE increases. Therefore, with increasing cycle number and $\mathrm{LAM_{pe}}$, the lower limit of the SoC is pushed higher.

Fig. 5f shows the particle surface concentrations ($c_{i,surf}/c_{i,max}$) in the PE (i = p) and NE (i = n) normalized by respective maximum concentrations. Two observations follow. First, the upper limit of $c_{n,surf}/c_{n,max}$ basically does not change, and so does the lower limit of $c_{p,surf}/c_{p,max}$. Second, in accordance with the increasing lower limit of $M_{cyc,n}$ in Fig. 5e, the lower limit of $c_{n,surf}/c_{n,max}$ keeps increasing with cycle number, and this increase drives its counterpart—the upper limit of $c_{p,surf}/c_{p,max}$ to increase slightly to meet the fixed lower cut-off voltage of 2.8 V (see the following discussion of Fig. 6 for more details). Note that this resultant slight increase in the PE particle does not conflict with the decreasing upper limit of total cyclable lithium $M_{cyc,p}$ in Fig. 5e because of the $\mathrm{LAM_{pe}}$.

The normalized surface concentration ($c_{i,surf}/c_{i,max}$) can be interpreted as the stoichiometry of the particle surface that determines the electrode potential. The variation of the two limit values of $c_{i,surf}/c_{i,max}$ reflects the degradation effect on the stoichiometry ranges of both electrodes and the match between them. We thus pick the first and last cycles and show in Fig. 6a the terminal voltage, PE potential, and NE potential versus the cell SoC of the discharge section (4th step in a cycle). Corresponding to the first observation from Fig. 5f, all three voltage curves of the last cycle start almost at the same points (fully-charged state) as their first-cycle counterparts, showing negligible differences between the first and last cycles. The same starting points, in spite of the continuing PE degradation and the $\mathrm{LAM_{pe}}$, can be explained as follows. The cyclable lithium $M_{cyc,p}$ in the PE at the starting point (lower limit in Fig. 5e) is zero for both the first and last cycles, and the concentration in the PE core takes the bottom value $c_{p,b}$ that equals the concentration c_s of trapped lithium in the shell. The progressive phase transition thus has no impact when the PE particle has zero cyclable lithium.

As discussed above, the $\mathrm{LAM_{pe}}$ results in earlier termination of the discharge. This is further reflected in Fig. 6a by the increase of the SoC lower limit from 0.04 in the first cycle to 0.36 in the last cycle. Since the NE has no degradation and its active material volume remains unchanged, the NE concentration and potential vary in the same pace with the cell SoC. Therefore, the NE potential curve (versus the cell SoC) of the last cycle simply overlays the first-cycle curve at the high-SoC side (Fig. 6a), showing a decrease of the NE potential at the end of discharge from the first to the last cycle. Accordingly, the NE particle stoichiometry at the end of discharge increases from 0.01 to 0.29 (Fig. 6b), corresponding to the second observation from Fig. 5f. The same lower cut-off value (2.8 V) is imposed to the terminal voltage—compare the solid and dashed purple lines (Fig. 6a); it follows that the PE potential is driven to be lower accordingly. A lower PE potential indicates higher surface concentration and stoichiometry, from 0.94 to 1.0 as shown in (Fig. 6b). In summary, Fig. 6b shows that the stoichiometry range of the NE particle during the discharge shrinks from $[0.81, 0.01]$ (the first cycle) to $[0.81, 0.29]$ (the last cycle), while the PE stoichiometry range expands from $[0.23, 0.94]$ to $[0.23, 1.0]$, leading to a re-match between the stoichiometry ranges.

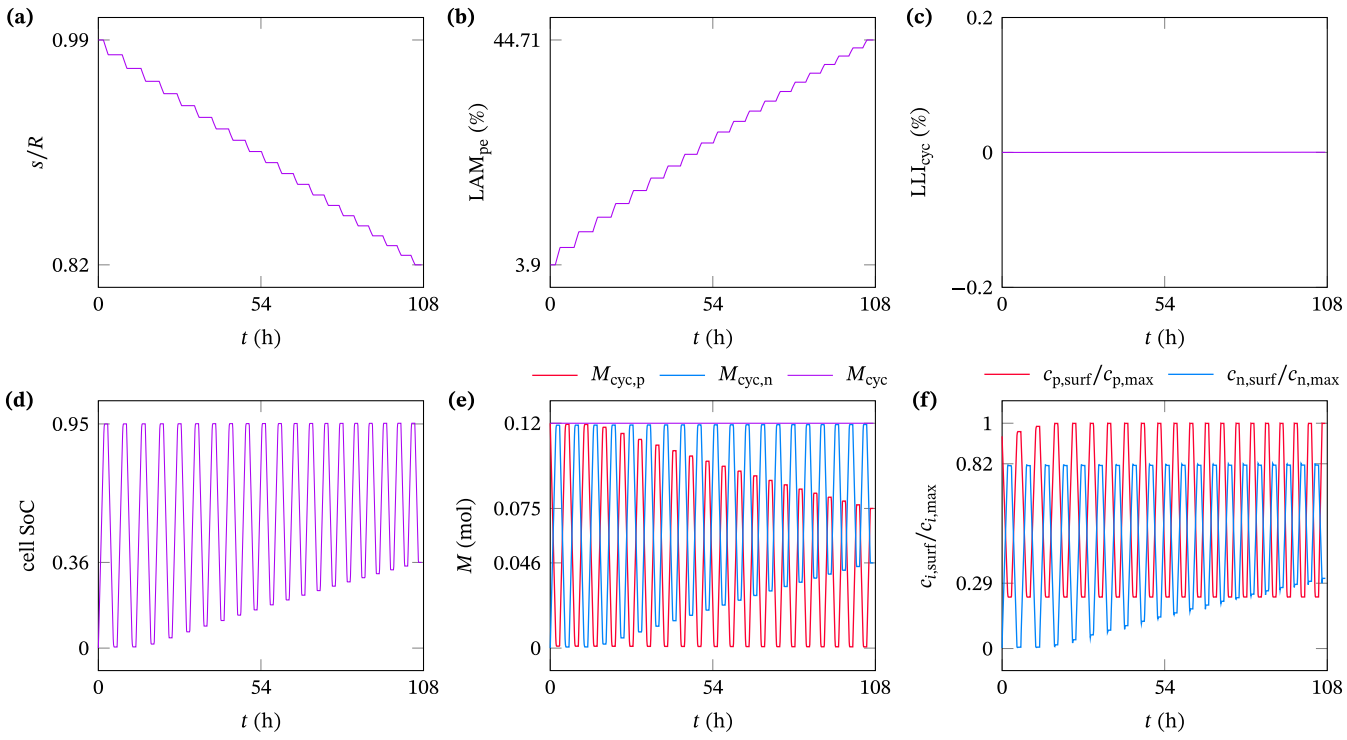

Fig. 5. Scenario I: effects of loss of PE active material (LAM_{pe}) on cell performance in cyclic ageing tests when the loss of cyclable lithium (LLI_{cyc}) is disabled. (a) Core–shell phase boundary (s/R), (e) total cyclable lithium (M_{cyc}) in both electrodes, cyclable lithium in the PE ($M_{cyc,p}$) and NE ($M_{cyc,n}$), and (f) normalized particle surface concentration/stoichiometry ($c_{i,surf}/c_{i,max}$). (For interpretation of the references to colour in this figure legend, the reader is referred to the web version of this article.)

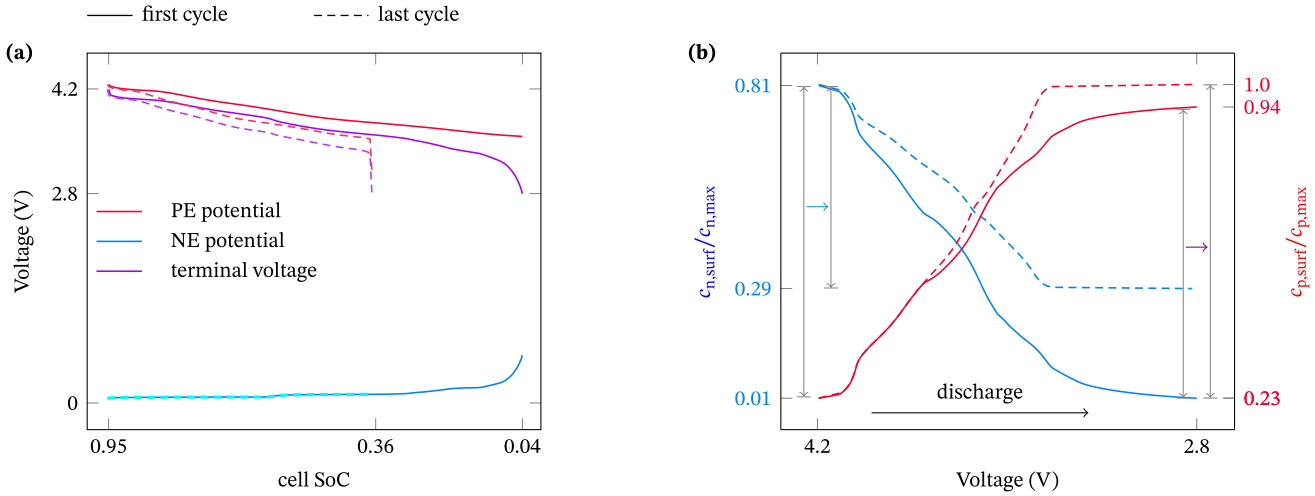

Fig. 6. Scenario I: (a) terminal voltage, PE potential, and NE potential versus the cell SoC in the discharge step of the first and last cycles; (b) shrinkage of the NE stoichiometry range and expansion of the PE stoichiometry range during discharge.

We can conclude that the capacity fade in this scenario is exclusively caused by the LAM_{pe} by lifting the SoC lower limit, and that the stoichiometry range of the PE particle is expanded in response to the shrinkage of the NE stoichiometry range, caused by the LAM_{pe}. We remark that, in spite of the null LLI_{cyc}, the LLI_{tot} is always increasing, in pace with the phase transition, but it is not a key factor. Rather, it is the LLI_{cyc} that matters, which is further discussed in scenario II.

Compared to scenario I, scenario II has additional LLI_{cyc} that is achieved by setting $c_s > c_{p,b}$. In Fig. 7c, the LLI_{cyc} increases with time (and degradation), which is cross-checked by the decreasing total cyclable lithium M_{cyc} in Fig. 7e. Note that we still keep $\rho = 0$ to have zero shell resistance and overpotential in this scenario.

Results of scenario II, as shown in Fig. 7, are similar to those of scenario I in Fig. 5, except for some differences caused by the introduced nonzero LLI_{cyc}. First, the direct effect of LLI_{cyc} is the decrease of the SoC upper limit with cycle number from 0.95 to 0.86 as shown in Fig. 7d, which can be explained by the same reasoning behind the constant upper limit at 0.95 in the case of zero LLI_{cyc}. The interpretation is also supported by Fig. 5e, in which the upper limit of cyclable lithium $M_{cyc,n}$ in the NE particle decreases at the same rate as the total cyclable lithium M_{cyc}. Second, although the SoC lower limit also increases with cycle number due to the LAM_{pe}, the increase amplitude (0.26) in Fig. 7d is smaller than that (0.36) in Fig. 5d. The smaller increase is exclusively due to the LLI_{cyc}, explained as follows. The LAM_{pe} in scenario II is the same as in scenario I (44.71% in Fig. 5b and Fig. 7b), and hence the decrease of the upper limit of the cyclable lithium $M_{cyc,p}$ in the PE, due to the LAM_{pe}, does not change from scenario I to scenario II (0.12 to

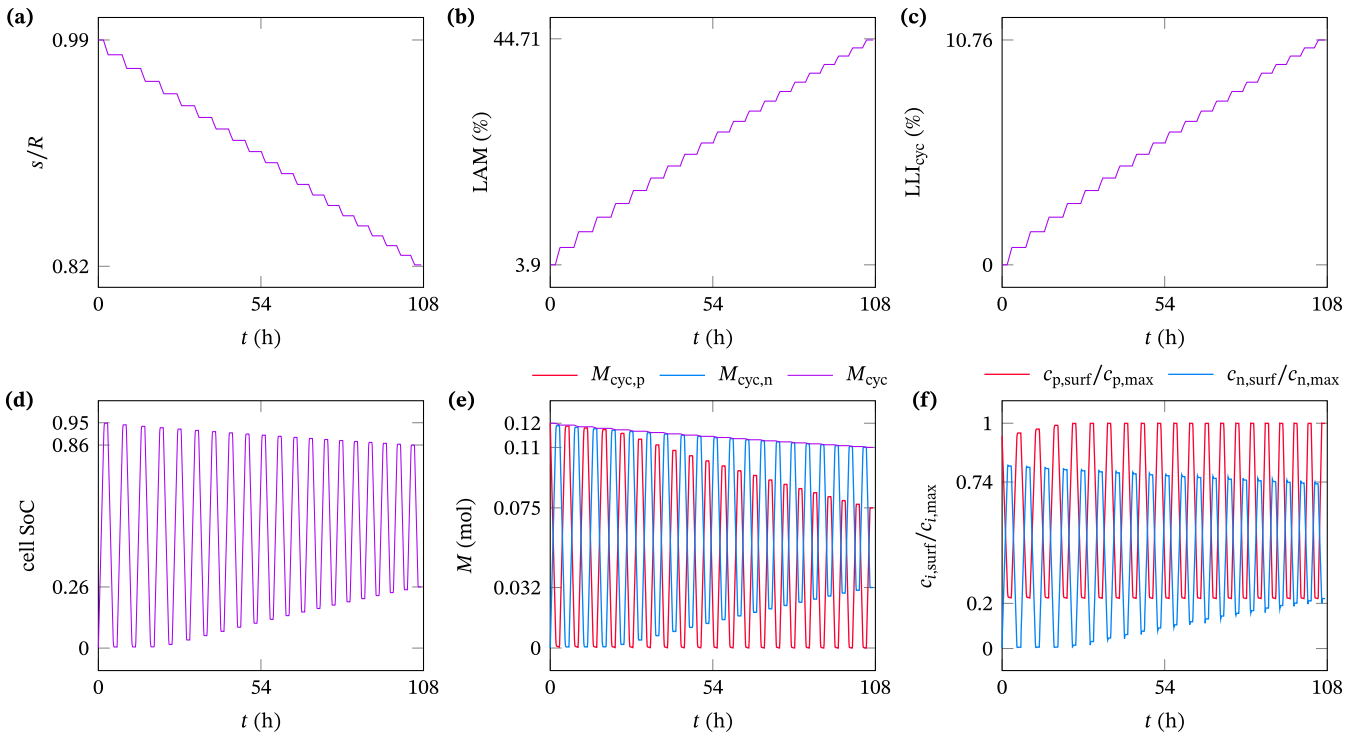

Fig. 7. Scenario II: collective effects of loss of PE active material (LAM_{pe}) and loss of cyclable lithium (LLI_{cyc}) on cell performance in cyclic ageing tests. (a) Core–shell phase boundary (s/R), (e) total cyclable lithium (M_{cyc}) in both electrodes, cyclable lithium in the PE ($M_{cyc,p}$) and NE ($M_{cyc,n}$), and (f) normalized particle surface concentration/stoichiometry ($c_{i,surf}/c_{i,max}$).

0.075 in both Fig. 5e and Fig. 7e). Thus, the lifting effect of the LAM_{pe} on the lower limit of $M_{cyc,n}$ should be the same in both scenarios; the difference is that in scenario II the decrease in total cyclable lithium M_{cyc} (i.e., the LLI_{cyc}) further drops the lower limit of $M_{cyc,n}$, thus counteracting the lifting effect of the LAM_{pe}.

The LLI_{cyc} shifts the upper limits of the SoC curve downwards: they basically remain constant in Fig. 5d but keep decreasing in Fig. 7d. However, the difference between the upper and lower SoC limits almost remains unchanged from scenario I to II, suggesting that no further capacity loss is caused by the LLI_{cyc}. The capacity loss is dominated by the LAM_{pe}, but this conclusion is exclusive to the setting in our simulation. Consider a scenario where the drop of M_{cyc} in Fig. 7e (the LLI_{cyc}) is larger than the decrease of the upper limit of $M_{cyc,p}$ due to the LAM_{pe}. In such a case, the LLI_{cyc} effect may dominate, leading to the capacity loss.

The downwards shifting of the SoC range in Fig. 7d is also reflected in Fig. 8a. Compared to Fig. 6a, the NE potential-SoC curve of the first cycle still overlap with part of the last-cycle curve, but slightly shifted to the low-SoC side. The PE potential and terminal voltage of the last cycle are accordingly shifted towards lower SoCs. The slight cell SoC decrease (0.95 to 0.86) from the first to the last cycle indicates that the NE is progressively less lithiated at the end of charge due to the LLI_{cyc}—see the change from 0.81 of the first cycle to 0.73 of the last cycle in Fig. 8b. The NE potential thus becomes higher and consequently leads to a higher PE potential under the constraint of fixed upper cut-off voltage (4.2 V). A higher PE potential at the end of charge further accelerates the PE degradation, acting as a positive feedback. In Fig. 8a, the increases of the NE and PE potentials are relatively slight because the OCP used for the SiC NE in our simulation is basically flat at high lithiation levels. As shown in Fig. 8b, the NE stoichiometry range is shrunk at both ends in this scenario: one by the LAM_{pe} and the other by the LLI_{cyc}. Accordingly, the PE stoichiometry range is expanded at both ends, and a re-match between their stoichiometry ranges occurs.

We remark that the above-discussed model prediction of higher PE potential and accelerated PE degradation is confirmed by experimental ageing studies [29] of graphite/NMC811 full cells. In Dose et al. [29], the progressively less lithiated graphite is attributed to electrode slippage, which is also named stoichiometry drift and related to the stoichiometry range re-match in our simulations. Our simulation results offer a possible explanation for the underlying cause of electrode slippage—the loss of cyclable lithium LLI_{cyc}.

Besides the LAM_{pe} and LLI_{cyc}, we further include the resistance of the shell layer and the resultant overpotential in scenario III. As indicated by Eq. (20), the shell overpotential depends on the current and the shell-layer thickness. The variation of the shell overpotential η_{shell} is shown in Fig. 9b: its amplitude increases with cycle number because of the growing shell-layer thickness (or decreasing phase boundary location s/R in Fig. 9a); its frequency and variation pattern follows the dynamics of the current.

The shell-layer overpotential impacts the terminal voltage, as can be seen in Eq. (33). During discharge, lithium enters the PE particle and the shell-layer overpotential η_{shell} is negative according to Eq. (20). The difference incurred by the negative η_{shell} is as follows. During discharge, the terminal voltage drops from the upper cut-off voltage of 4.2 V. In Fig. 6a and Fig. 8a, the drop of the terminal voltage in the beginning of discharge is the same for the first and last cycles, as caused by reaction overpotential. However, the terminal-voltage drop in Fig. 10a for the last cycle is up to 0.6 V, mostly contributed by the shell overpotential (0.49 V). The terminal voltage continues to stay at the low level during the whole discharge, diminishing the available power of the cell.

Furthermore, since the lower cut-off voltage is fixed, the extra shell overpotential leads to earlier termination of the discharge, i.e., the discharge ends at a higher SoC value (0.27 in Fig. 8a versus 0.33 in Fig. 10a), exacerbating the lifting effect by the LAM_{pe}. This means the shell overpotential further narrows down the SoC range from the bottom side (end of discharge): the lower limit increases from 0.26 (Fig. 7d) without the shell overpotential to 0.32 (Fig. 9d) with overpotential. Accordingly, the surface stoichiometry of the NE particle at the end of discharge increases from 0.2 (Fig. 8b) to 0.25 (Fig. 10b), suggesting a further shrinkage of the NE stoichiometry range from scenario II to III caused by the shell overpotential. Note that the minor

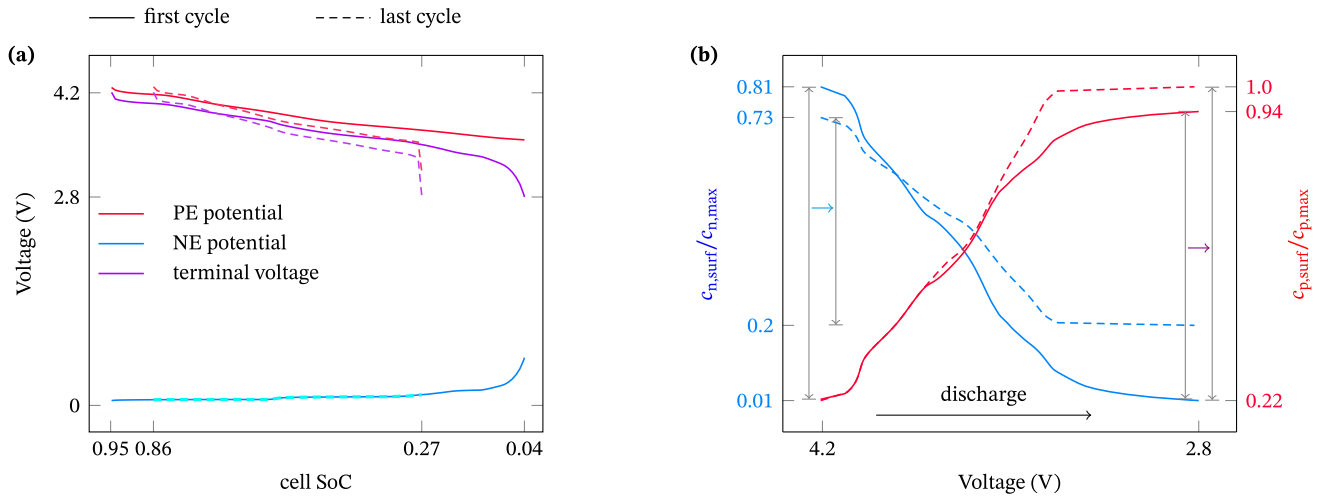

Fig. 8. Scenario II: (a) terminal voltage, PE potential, and NE potential versus the cell SoC in the discharge step of the first and last cycles; (b) shrinkage of the NE stoichiometry range and expansion of the PE stoichiometry range during discharge.

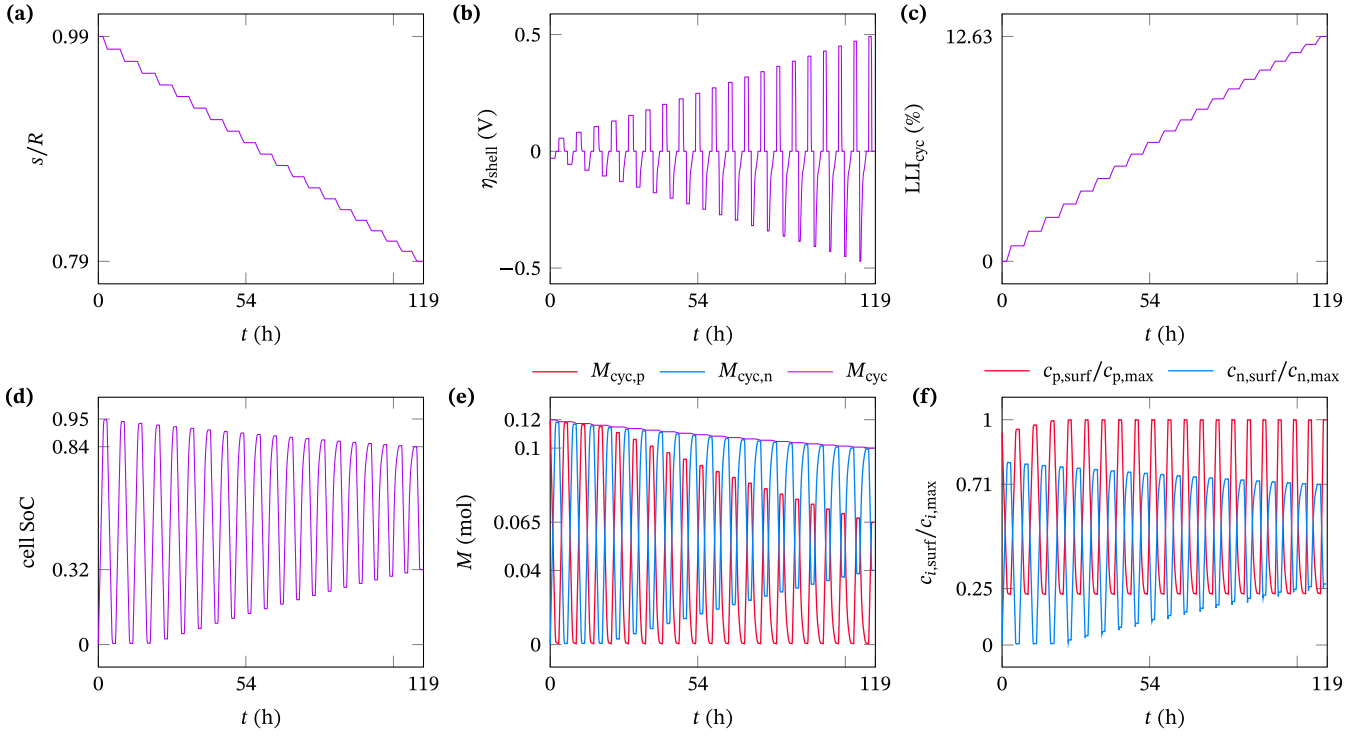

Fig. 9. Scenario III: collective effects of loss of PE active material (LAM_{pe}), loss of cyclable lithium (LLI_{cyc}), and shell-layer resistance on cell performance in cyclic ageing tests. (a) core–shell phase boundary (s/R), (b) overpotential (η_{shell}) across the shell layer, (e) total cyclable lithium (M_{cyc}) in both electrodes, cyclable lithium in the PE ($M_{cyc,p}$) and NE ($M_{cyc,n}$), and (f) normalized particle surface concentration/stoichiometry ($c_{i,surf}/c_{i,max}$).

difference in the SoC lower limits between Fig. 10a (0.33) and Fig. 9d (0.32) is because the voltage control following the discharge slightly pulls down the SoC. The same phenomena and reasoning apply to scenario II in Fig. 8a and Fig. 7d.

The SoC upper limit (0.84) in Fig. 9d is also lower than that (0.86) in Fig. 7d. This small drop is mainly caused by a greater LLI_{cyc}—12.63% in Fig. 9c vs 10.76% in Fig. 7c. During charge, the shell overpotential makes the cell further away from equilibrium when the upper cut-off voltage is reached, leading to a longer voltage control afterwards with degradation occurring. The longer the degradation lasts, the higher the LLI_{cyc} value and the lower the s/R value (0.82 → 0.79 from scenario II to III). The longer voltage control agrees with the fact that a longer time (119 h in Fig. 9) to complete 20 cycles in scenario III than the 108 h (Fig. 7) used in scenario II. In summary, the extra shell overpotential leads to further shrinkage of the cell SoC range (Fig. 8a vs Fig. 10a) and shrinkage of the NE stoichiometry range (Fig. 8b vs Fig. 10b) from both ends. The shell overpotential also depresses the cell power by diminishing the terminal voltage.

Finally, we plot the discharge-capacity fade for all three scenarios in Fig. 11. The difference between scenario I and II is negligible because, as discussed above, the LAM_{pe} effect is dominant over the LLI_{cyc} effect such that the additional LLI_{cyc} does not result in extra capacity loss. The capacity in scenario III drops faster because of the extra shell-layer overpotential causing further shrinkage of the cell SoC range.

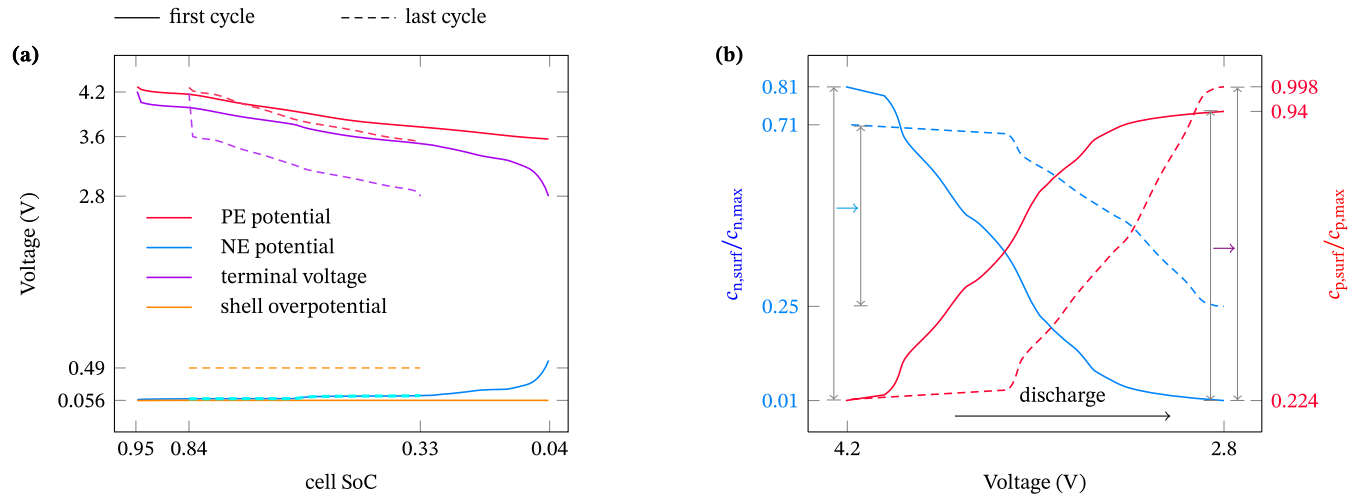

Fig. 10. Scenario III: (a) terminal voltage, PE potential, and NE potential versus the cell SoC in the discharge step of the first and last cycles; (b) shrinkage of the NE stoichiometry range and expansion of the PE stoichiometry range during discharge.

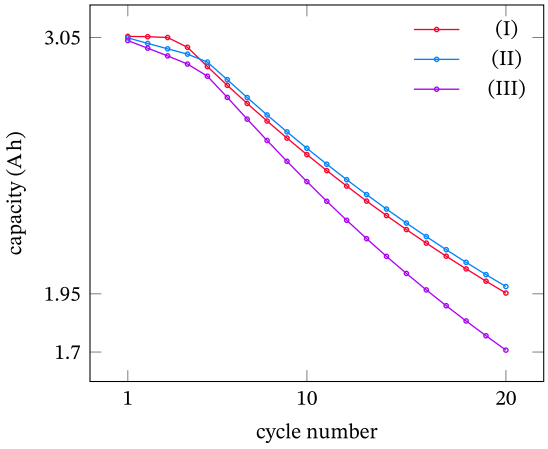

Fig. 11. Discharge-capacity fade for scenario I considering the LAM_{pe}, scenario II considering the LAM_{pe} and the LLI_{cyc}, and scenario III considering the LAM_{pe}, the LLI_{cyc}, and shell-layer resistance.

4.3. Degradation inhomogeneity in through-cell direction

In the previous section, we present the degradation in the average sense and disregard its variation in the direction of electrode thickness. Here we present the degradation inhomogeneity across the electrode thickness caused by a constant-current charge at a 1 C rate followed by a voltage control and a half-hour rest. In this case, the particle degradation model is implemented within the DFN model in PyBaMM.

The current variation, in accordance with the specified protocol, is shown in Fig. 12a. In particular, the current decreasing in magnitude results from the voltage control. During the procedure, we pick four time instants, corresponding to points A–D in Fig. 12a, and show the positive core surface concentration $c_{p,surf}$, phase boundary location s/R, and the loss of PE active material LAM_{pe} in subplots b–d, respectively. The three quantities in b–d not only vary with the time but also depend on the depth x through the PE relative to the current collector at the NE side (98.7 μm is the thickness of the NE and separator). At the initial time (point A), the lithium concentration is set to be uniform across the electrode and inside the core of each PE particle, and thus the core surface concentration is constant in the x direction (Fig. 12b). The phase boundary location (Fig. 12c) is also set to be constant initially in the whole electrode. During the constant-current charge and voltage control, lithium are removed from the PE and inserted into the NE, leading to a continuous decrease of the PE core (surface) concentration. In particular, the surface concentration is lower at the PE-separator boundary, and this is because the interfacial current density is larger for PE particles closer to the separator where the resistance for current flow is smaller [30]. By the time at point B, the PE core surface concentration has dropped dramatically to the extent that the surface concentration at the separator side ($x = 98.7$ μm in Fig. 12b) is lower than the phase-transition threshold value. Hence, the phase boundary moves inwards for particles close to the separator; the lower the surface concentration, the larger extent to which the phase transition occurs and the lower the s/R value. The surface concentrations of particles close to the current-collector side are still above the phase-transition threshold value, and thus there is yet no phase transition at higher x values in Fig. 12c. After point B, the cell charge gradually fades until the current vanishes. Accordingly, we just observe a slight decrease of the surface concentration from B to C and D in Fig. 12b. However, the phase boundary location s/R continues to decrease (B→C→D) as the surface concentration remains low. The low surface concentration enables the phase transition to proceed across the whole electrode, and the speed of phase change (time rate of s/R in Eq. (13)) is basically uniform in the x direction. Therefore, s/R as a function of x shifts downwards as a whole in Fig. 12c. The LAM_{pe} at the four time instants in Fig. 12d shows similar profiles and behavior to the phase boundary s/R because of the definition (14).

We further show the degradation inhomogeneity effect on the oxygen concentration. Unlike the three variables in Fig. 12b–d, the oxygen concentration c_o is solved in the shell phase of a PE particle that presents across the entire electrode thickness. Therefore, c_o varies in the radial direction of a PE particle, and this variation is different in particles at different locations in the through-electrode direction. Fig. 13 shows the oxygen concentration contours at the four chosen time instants. The horizontal axis (x) denotes the electrode thickness direction, and the vertical axis (r) represents the radial direction of a particle. Note that the shell thickness ($R - s$) varies with time and with the coordinate x (Fig. 12c), and that the heights of the four subplots do not represent the actual shell thickness but are scaled accordingly. Initially at point A, the oxygen concentration is uniform in both directions and stays null as no phase transition occurs everywhere. At point B, the phase transition starts to occur at the separator side (lower x values; see the blue line B in Fig. 12c), releasing the oxygen stored in the core into the shell. Once generated at the phase boundary ($r = s$), the oxygen diffuses out through the shell, forming a concentration gradient in the r direction. A concentration decay is also seen in the x direction because at this point there is still no phase transition at locations away

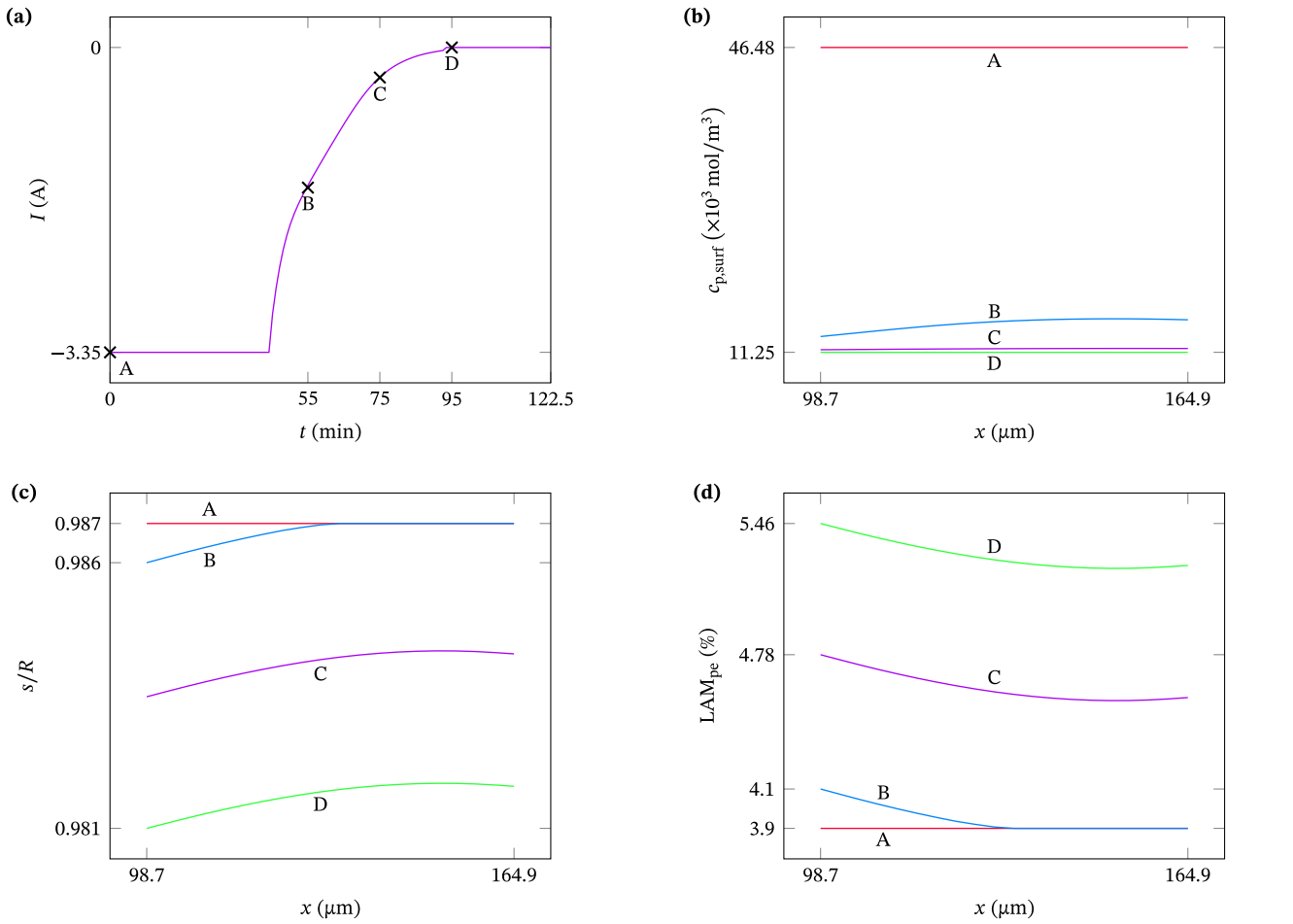

Fig. 12. Degradation inhomogeneity along the electrode thickness direction in a numerical test of cell charge followed by voltage control and rest. The current I for the test protocol is shown in subplot (a) as a function of time in minutes. (b) Positive core surface concentration $c_{p,surf}$, (c) phase boundary location s/R, and (d) loss of PE active material LAM_{pe} at four time instants corresponding to four points A–D in (a). The PE is represented by $98.7 \leq x \leq 164.9\,\mu m$ in the thickness direction.

from the separator (higher x values). This explains the concentration hot point in the lower-left corner. With the phase transition spreading from the separator side (B) to the whole electrode (C and D), the generated oxygen is present throughout the whole electrode, and the longer the phase transition undergoes, the higher value of the oxygen concentration (C vs D). Meanwhile, the oxygen concentration gradient remains in the r direction due to the boundary condition of zero oxygen at the shell surface.

4.4. Remarks

The results discussed above are for the degradation of the positive electrode only, and caution should be taken when applying the learnings to a full cell. The model predictions cannot and should not be compared directly to full-cell behavior where the negative-electrode and electrolyte regions will both contribute towards degradation—the evolution of LLI, stoichiometry drift, capacity fade, and impedance changes. If the degradation experiments or the field data include events that allow degradation mode analysis to be periodically conducted, e.g. a slow constant-current charge/discharge, the predicted LAM_{pe} can be compared directly; however, the LLI_{cyc} would still be a combination of both positive and negative electrode processes. To reproduce the full-cell behavior, the model presented here would need to be coupled with sufficient models of other degradation mechanisms describing the negative-electrode [31] and electrolyte regions [32].

To realize the full usefulness of the approach, future work should combine experiments including degradation mode analysis with models coupling all the degradation mechanisms that are relevant for a particular cell and use case. This would allow multiple degradation pathways through the degradation space [2] to be explored, with the degradation mode analysis compared to the model predictions to help interpret what has happened inside the cell. The goal should be that such an experimentally validated model should be capable of predicting how long lithium-ion batteries will last as a function of both how they

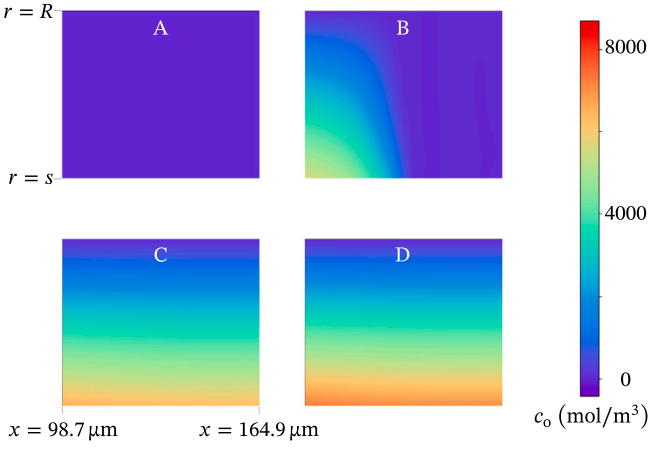

Fig. 13. Oxygen concentration c_o contour at four time instants (t = 0, 55, 75, 95 min) corresponding to the four points A–D marked in Fig. 12a, respectively.

are made and how they are used. The approach could also help establish if there are observable differences in degradation mode evolution for different combinations of degradation mechanisms under different conditions and different chemistries, therefore contributing towards understanding the limits of observability for in-operando diagnostic techniques.

5. Conclusion

We developed a shrinking-core particle model to describe the degradation mechanism of phase transition for high-nickel PEs and presented a two-step strategy to understand the degradation effects. We have shown how the progress of the phase transition directly results in the primary degradation modes of loss of PE active material (LAM_{pe}), loss of lithium inventory (LLI_{tot} and LLI_{cyc}), and additional shell-layer resistance (Section 4.1); the primary degradation modes then deteriorate the cell performance in terms of capacity and power (Section 4.2).

It is found that the LAM_{pe} lifts the lower limit of the SoC range by terminating the discharge earlier, while the LLI_{cyc} suppresses the upper limit of the SoC range; in our simulated cases, the LAM_{pe} is the dominant factor contributing to the capacity loss. The shell-layer overpotential shrinks the SoC range from both ends, leading to a power reduction and further capacity fade under a fixed-voltage-window operation. The LAM_{pe} and LLI_{cyc} narrow down the stoichiometry range of the NE and consequently expand the PE stoichiometry range due to the fixed-voltage window. Due to the flat NE open circuit potential at high lithiation, the increase of PE potential at the end of charge is slight; for a NE with steeper potential curve, we expect a noticeable PE potential increase caused by the LLI_{cyc}, leading to positive feedback and accelerating the PE degradation.

We find that it is the LLI_{cyc}, not LLI_{tot}, that impacts the cell performance, and thus we suggest to explicitly differentiate the cyclable lithium from the total lithium in the calculation of LLI. LLI_{tot} always occurs during the phase transition, but this is not the case for LLI_{cyc}; the LLI_{cyc} depends on the concentration of lithium (c_s) trapped in the degraded materials, which is assumed as a constant in our model. Thus, the calibration of parameter c_s against experiments is key to identifying the LLI effects.

The study of LAM and LLI effects on capacity fade has offered insights into experimental diagnosis of battery degradation modes. Specifically, we can differentiate the contribution to degradation by LAM from that by LLI according to the cell SoC variation curve and especially its change pattern. With the primary degradation modes captured, the model can qualitatively reproduce experimentally observed phenomena (e.g., capacity fade and stoichiometry drift).

Challenges remain in model calibration and validation against specifically designed experiments, as the model presented here is for the positive electrode degradation only. The ultimate usefulness of the proposed model will manifest when it is coupled with other models for degradation in the negative-electrode and electrolyte regions, and when validated with degradation experiments specifically designed to identify different pathways through the degradation space. This work is therefore an important milestone on the trajectory towards a universal lithium-ion battery degradation model capable of predicting how long lithium-ion batteries will last as a function of both how they are made and how they are used.

CRediT authorship contribution statement

Mingzhao Zhuo: Conceptualization, Methodology, Software, Validation, Data curation, Writing – original draft, Writing – review & editing, Visualization. **Gregory Offer:** Conceptualization, Methodology, Writing – review & editing, Supervision, Funding acquisition. **Monica Marinescu:** Conceptualization, Methodology, Writing – review & editing, Supervision, Funding acquisition.

Declaration of competing interest

The authors declare that they have no known competing financial interests or personal relationships that could have appeared to influence the work reported in this paper.

Data availability

The data leading to the findings of this study, including model derivation and implementation, are openly available in the public repository at https://github.com/mzzhuo/PE_degradation.

Acknowledgments

The research leading to these results has received funding from the Innovate UK through the WIZer Batteries project (grant number 104427) and EPSRC, UK Faraday Institution Multi-Scale Modelling project (EP/S003053/1, grant number FIRG003). The support from PyBaMM development team is appreciated in our model implementation within PyBaMM.

Appendix. Numerical implementation in pybamm

The particle degradation model is implemented as a submodel in PyBaMM [3], which is an open-source python programming package aimed at solving physics-based electrochemical models (differential algebraic equations). The submodel can then be called by the Single Particle Model and Doyle–Fuller–Newman model available in PyBaMM, in place of the original particle model that only considers fickian diffusion. The nondimensionalization of equations and boundary conditions and implementation (codes) can be found via the link https://github.com/mzzhuo/PE_degradation.

Regarding the degradation particle model, there are two numerical challenges to address. The first is that the computational domains of the core and shell are changing with time due to the moving phase boundary. To fix this problem, we follow the same numerical trick as in Refs. [13,22] and define two new spatial variables η and χ for the core and shell, respectively:

$$\eta = \frac{r}{s}, \quad \chi = \frac{r-s}{R-s}, \tag{A.1}$$

where r is the spatial coordinate in the radial direction, s denotes the phase boundary location, and R is the particle radius (see Fig. 2). Now the computational domains of the core and shell both reduce to $\eta, \chi \in [0, 1]$.

The second is the discretization of the Robin-type boundary condition (10). Referring to Fig. A.14, the discretized version can be expressed as

$$\dot{s}\left(c_s - c_{p,s}\right) - D_p \frac{2}{s} \frac{c_{p,s} - c_{p,N}}{l_1} - (R/s)^2 \frac{j_p}{F} = 0. \tag{A.2}$$

The boundary value $c_{p,s}$ is solved from Eq. (A.2) and used to express the boundary flux term (the middle term), and then the flux term is applied in the same way as the normal Neumann boundary condition. The same procedure applies to the boundary condition (12) for oxygen diffusion.

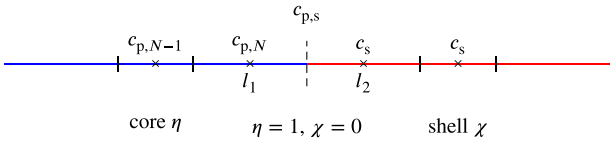

Fig. A.14. Schematic of discretization of the moving phase boundary condition (10). Parameter $c_{p,s}$ denotes the value of concentration c_p at the core–shell phase boundary, and N is the number of cells after discretization using the finite volume method.

References

[1] D.-S. Ko, J.-H. Park, B.Y. Yu, D. Ahn, K. Kim, H.N. Han, W.S. Jeon, C. Jung, A. Manthiram, Degradation of high-nickel-layered oxide cathodes from surface to bulk: A comprehensive structural, chemical, and electrical analysis, Adv. Energy Mater. 10 (36) (2020) 2001035, http://dx.doi.org/10.1002/aenm.202001035.

[2] J.S. Edge, S. O'Kane, R. Prosser, N.D. Kirkaldy, A.N. Patel, A. Hales, A. Ghosh, W. Ai, J. Chen, J. Yang, S. Li, M.-C. Pang, L.B. Diaz, A. Tomaszewska, M.W. Marzook, K.N. Radhakrishnan, H. Wang, Y. Patel, B. Wu, G.J. Offer, Lithium ion battery degradation: what you need to know, Phys. Chem. Chem. Phys. 23 (14) (2021) 8200–8221, http://dx.doi.org/10.1039/d1cp00359c.

[3] V. Sulzer, S.G. Marquis, R. Timms, M. Robinson, S.J. Chapman, Python battery mathematical modelling (PyBaMM), J. Open Res. Softw. 9 (2021) http://dx.doi.org/10.5334/jors.309.

[4] M.D. Radin, S. Hy, M. Sina, C. Fang, H. Liu, J. Vinckeviciute, M. Zhang, M.S. Whittingham, Y.S. Meng, A.V. der Ven, Narrowing the gap between theoretical and practical capacities in Li-ion layered oxide cathode materials, Adv. Energy Mater. 7 (20) (2017) 1602888, http://dx.doi.org/10.1002/aenm.201602888.

[5] F. Lin, I.M. Markus, D. Nordlund, T.-C. Weng, M.D. Asta, H.L. Xin, M.M. Doeff, Surface reconstruction and chemical evolution of stoichiometric layered cathode materials for lithium-ion batteries, Nature Commun. 5 (1) (2014) http://dx.doi.org/10.1038/ncomms4529.

[6] N. Li, M. Sun, W.H. Kan, Z. Zhuo, S. Hwang, S.E. Renfrew, M. Avdeev, A. Huq, B.D. McCloskey, D. Su, W. Yang, W. Tong, Layered-rocksalt intergrown cathode for high-capacity zero-strain battery operation, Nature Commun. 12 (1) (2021) http://dx.doi.org/10.1038/s41467-021-22527-z.

[7] R. Jung, M. Metzger, F. Maglia, C. Stinner, H.A. Gasteiger, Oxygen release and its effect on the cycling stability of $LiNi_xMn_yCo_zO_2$ (NMC) cathode materials for Li-ion batteries, J. Electrochem. Soc. 164 (7) (2017) A1361–A1377, http://dx.doi.org/10.1149/2.0021707jes.

[8] S.S. Zhang, Understanding of performance degradation of $LiNi_{0.80}Co_{0.10}Mn_{0.10}O_2$ cathode material operating at high potentials, J. Energy Chem. 41 (2020) 135–141, http://dx.doi.org/10.1016/j.jechem.2019.05.013.

[9] J.A. Gilbert, I.A. Shkrob, D.P. Abraham, Transition metal dissolution, ion migration, electrocatalytic reduction and capacity loss in Lithium-ion full cells, J. Electrochem. Soc. 164 (2) (2017) A389–A399, http://dx.doi.org/10.1149/2.1111702jes.

[10] R. Jung, F. Linsenmann, R. Thomas, J. Wandt, S. Solchenbach, F. Maglia, C. Stinner, M. Tromp, H.A. Gasteiger, Nickel, manganese, and cobalt dissolution from Ni-rich NMC and their effects on NMC622-graphite cells, J. Electrochem. Soc. 166 (2) (2019) A378–A389, http://dx.doi.org/10.1149/2.1151902jes.

[11] Z. Ruff, C. Xu, C.P. Grey, Transition metal dissolution and degradation in NMC811-graphite electrochemical cells, J. Electrochem. Soc. 168 (6) (2021) 060518, http://dx.doi.org/10.1149/1945-7111/ac0359.

[12] J. Lai, J. Zhang, Z. Li, Y. Xiao, W. Hua, Z. Wu, Y. Chen, Y. Zhong, W. Xiang, X. Guo, Structural elucidation of the degradation mechanism of nickel-rich layered cathodes during high-voltage cycling, Chem. Commun. 56 (36) (2020) 4886–4889, http://dx.doi.org/10.1039/d0cc00327a.

[13] A. Ghosh, J.M. Foster, G. Offer, M. Marinescu, A shrinking-core model for the degradation of high-nickel cathodes (NMC811) in Li-ion batteries: Passivation layer growth and oxygen evolution, J. Electrochem. Soc. 168 (2) (2021) 020509, http://dx.doi.org/10.1149/1945-7111/abdc71.

[14] X. Lin, J. Park, L. Liu, Y. Lee, A.M. Sastry, W. Lu, A comprehensive capacity fade model and analysis for Li-ion batteries, J. Electrochem. Soc. 160 (10) (2013) A1701–A1710, http://dx.doi.org/10.1149/2.040310jes.

[15] A. Jana, G.M. Shaver, R.E. García, Physical, on the fly, capacity degradation prediction of $LiNiMnCoO_2$-graphite cells, J. Power Sources 422 (2019) 185–195, http://dx.doi.org/10.1016/j.jpowsour.2019.02.073.

[16] T. Li, X.-Z. Yuan, L. Zhang, D. Song, K. Shi, C. Bock, Degradation mechanisms and mitigation strategies of nickel-rich NMC-based lithium-ion batteries, Electrochem. Energy Rev. 3 (1) (2019) 43–80, http://dx.doi.org/10.1007/s41918-019-00053-3.

[17] T. Sasaki, T. Nonaka, H. Oka, C. Okuda, Y. Itou, Y. Kondo, Y. Takeuchi, Y. Ukyo, K. Tatsumi, S. Muto, Capacity-fading mechanisms of $LiNiO_2$-based lithium-ion batteries, J. Electrochem. Soc. 156 (4) (2009) A289, http://dx.doi.org/10.1149/1.3076136.

[18] S.-K. Jung, H. Gwon, J. Hong, K.-Y. Park, D.-H. Seo, H. Kim, J. Hyun, W. Yang, K. Kang, Understanding the degradation mechanisms of $LiNi_{0.5}Co_{0.2}Mn_{0.3}O_2$ cathode material in lithium ion batteries, Adv. Energy Mater. 4 (1) (2014) 1300787, http://dx.doi.org/10.1002/aenm.201300787.

[19] R. Jung, R. Morasch, P. Karayaylali, K. Phillips, F. Maglia, C. Stinner, Y. Shao-Horn, H.A. Gasteiger, Effect of ambient storage on the degradation of Ni-rich positive electrode materials (NMC811) for Li-ion batteries, J. Electrochem. Soc. 165 (2) (2018) A132–A141, http://dx.doi.org/10.1149/2.0401802jes.

[20] M. Safari, M. Morcrette, A. Teyssot, C. Delacourt, Multimodal physics-based aging model for life prediction of Li-ion batteries, J. Electrochem. Soc. 156 (3) (2009) A145, http://dx.doi.org/10.1149/1.3043429.

[21] S.-M. Bak, E. Hu, Y. Zhou, X. Yu, S.D. Senanayake, S.-J. Cho, K.-B. Kim, K.Y. Chung, X.-Q. Yang, K.-W. Nam, Structural changes and thermal stability of charged $LiNi_xMn_yCo_zO_2$ cathode materials studied by combined in situ time-resolved XRD and mass spectroscopy, ACS Appl. Mater. Interfaces 6 (24) (2014) 22594–22601, http://dx.doi.org/10.1021/am506712c.

[22] Q. Zhang, R.E. White, Moving boundary model for the discharge of a $LiCoO_2$ electrode, J. Electrochem. Soc. 154 (6) (2007) A587, http://dx.doi.org/10.1149/1.2728733.

[23] R. Jung, P. Strobl, F. Maglia, C. Stinner, H.A. Gasteiger, Temperature dependence of oxygen release from $LiNi_{0.6}Co_{0.2}Mn_{0.2}O_2$ (NMC622) cathode materials for li-ion batteries, J. Electrochem. Soc. 165 (11) (2018) A2869–A2879, http://dx.doi.org/10.1149/2.1261811jes.

[24] L. Cai, R.E. White, Mathematical modeling of a lithium ion battery with thermal effects in COMSOL Inc. multiphysics (MP) software, J. Power Sources 196 (14) (2011) 5985–5989, http://dx.doi.org/10.1016/j.jpowsour.2011.03.017.

[25] S.G. Marquis, V. Sulzer, R. Timms, C.P. Please, S.J. Chapman, An asymptotic derivation of a single particle model with electrolyte, J. Electrochem. Soc. 166 (15) (2019) A3693–A3706, http://dx.doi.org/10.1149/2.0341915jes.

[26] B. Tjaden, S.J. Cooper, D.J. Brett, D. Kramer, P.R. Shearing, On the origin and application of the Bruggeman correlation for analysing transport phenomena in electrochemical systems, Curr. Opin. Chem. Eng. 12 (2016) 44–51, http://dx.doi.org/10.1016/j.coche.2016.02.006.

[27] J. Sturm, A. Rheinfeld, I. Zilberman, F. Spingler, S. Kosch, F. Frie, A. Jossen, Modeling and simulation of inhomogeneities in a 18650 nickel-rich, silicon-graphite lithium-ion cell during fast charging, J. Power Sources 412 (2019) 204–223, http://dx.doi.org/10.1016/j.jpowsour.2018.11.043.

[28] C. Capiglia, Y. Saito, H. Kageyama, P. Mustarelli, T. Iwamoto, T. Tabuchi, H. Tukamoto, ^7Li and ^{19}F diffusion coefficients and thermal properties of non-aqueous electrolyte solutions for rechargeable lithium batteries, J. Power Sources 81–82 (1999) 859–862, http://dx.doi.org/10.1016/s0378-7753(98)00237-7.

[29] W.M. Dose, C. Xu, C.P. Grey, M.F.D. Volder, Effect of anode slippage on cathode cutoff potential and degradation mechanisms in Ni-rich Li-ion batteries, Cell Rep. Phys. Sci. 1 (11) (2020) 100253, http://dx.doi.org/10.1016/j.xcrp.2020.100253.

[30] Z. Geng, S. Wang, M.J. Lacey, D. Brandell, T. Thiringer, Bridging physics-based and equivalent circuit models for lithium-ion batteries, Electrochim. Acta 372 (2021) 137829, http://dx.doi.org/10.1016/j.electacta.2021.137829.

[31] S.E.J. O'Kane, W. Ai, G. Madabattula, D. Alonso-Alvarez, R. Timms, V. Sulzer, J.S. Edge, B. Wu, G.J. Offer, M. Marinescu, Lithium-ion battery degradation: how to model it, Phys. Chem. Chem. Phys. 24 (13) (2022) 7909–7922, http://dx.doi.org/10.1039/d2cp00417h.

[32] R. Li, S. O'Kane, M. Marinescu, G.J. Offer, Modelling solvent consumption from SEI layer growth in lithium-ion batteries, J. Electrochem. Soc. 169 (6) (2022) 060516, http://dx.doi.org/10.1149/1945-7111/ac6f84.